

Dysregulated Ca²⁺ signaling, fluid secretion, and mitochondrial function in a mouse model of early Sjögren's disease

Kai-Ting Huang¹, Larry E Wagner¹, Takahiro Takano¹, Xiao-Xuan Lin¹, Harini Bagavant², Umesh Deshmukh², David I Yule^{1*}

¹Department of Pharmacology and Physiology, University of Rochester, Rochester, United States; ²Arthritis and Clinical Immunology, Oklahoma Medical Research Foundation, Oklahoma City, United States

Abstract The molecular mechanisms leading to saliva secretion are largely established, but factors that underlie secretory hypofunction, specifically related to the autoimmune disease Sjögren's syndrome (SS) are not fully understood. A major conundrum is the lack of association between the severity of salivary gland immune cell infiltration and glandular hypofunction. SS-like disease was induced by treatment with DMXAA, a small molecule agonist of murine STING. We have previously shown that the extent of salivary secretion is correlated with the magnitude of intracellular Ca²⁺ signals (Takano et al., 2021). Contrary to our expectations, despite a significant reduction in fluid secretion, neural stimulation resulted in enhanced Ca²⁺ signals with altered spatiotemporal characteristics in vivo. Muscarinic stimulation resulted in reduced activation of the Ca²⁺-activated Cl⁻ channel, TMEM16a, although there were no changes in channel abundance or absolute sensitivity to Ca²⁺. Super-resolution microscopy revealed a disruption in the colocalization of Inositol 1,4,5-trisphosphate receptor Ca²⁺ release channels with TMEM16a, and channel activation was reduced when intracellular Ca²⁺ buffering was increased. These data indicate altered local peripheral coupling between the channels. Appropriate Ca²⁺ signaling is also pivotal for mitochondrial morphology and bioenergetics. Disrupted mitochondrial morphology and reduced oxygen consumption rate were observed in DMXAA-treated animals. In summary, early in SS disease, dysregulated Ca²⁺ signals lead to decreased fluid secretion and disrupted mitochondrial function contributing to salivary gland hypofunction.

*For correspondence:
david_yule@urmc.rochester.edu

Competing interest: The authors declare that no competing interests exist.

Funding: See page 24

Preprint posted
19 March 2024

Sent for Review
19 March 2024

Reviewed preprint posted
24 May 2024

Reviewed preprint revised
22 August 2024

Version of Record published
11 September 2024

Reviewing Editor: Murali Prakriya, Northwestern University, United States

© Copyright Huang et al. This article is distributed under the terms of the [Creative Commons Attribution License](https://creativecommons.org/licenses/by/4.0/), which permits unrestricted use and redistribution provided that the original author and source are credited.

eLife assessment

This manuscript presents **important** observations on the early changes that occur in calcium signaling, TMEM16a channel activation, and mitochondrial dysfunction in salivary gland cells in a murine model of autoimmune Sjögren's disease. The study reports that in response to DMXAA treatment which induces a murine model of Sjögren's disease, salivary gland cells show significant changes in saliva release, calcium signaling, TMEM16a activation, mitochondrial function, and sub-cellular morphology of the endoplasmic reticulum. The work is **compelling** and will be of strong interest to physiologists working on secretion, calcium signaling, and mitochondria.

Introduction

Saliva plays crucial roles in oral health, including lubricating the mouth, maintaining pH balance, defense against microorganisms, aiding taste, and initiating digestion of macronutrients (*Humphrey and Williamson, 2001; Carpenter, 2013; Pedersen et al., 2018*). Saliva is produced primarily by

three major salivary glands; the submandibular gland (SMG), parotid gland (PG), sublingual gland (SLG), and some minor glands in the lower lip, tongue, and cheek. Saliva is generated in secretory acinar cells, with its content adjusted by ducts before reaching the mouth. The acinar cells are fundamental to the production of the primary salivary secretion (*de Paula et al., 2017*). The fluid secretion process is driven by the trans-epithelial movement of Cl^- across acinar cells. To accomplish vectorial movement of Cl^- , acinar cells are polarized such that the basolateral plasma membrane (PM) faces the interstitium and is adjacent to blood vessels, while the apical PM forms a lumen with the distinct PM regions physically segregated by tight-junctional complexes. At the basolateral PM, Cl^- is transported into the acinar cell cytoplasm against their electrochemical gradient via the $\text{Na}^+/\text{K}^+/\text{2Cl}^-$ cotransporter, (NKCC1). Following mastication or the experience of the taste and the smell of food, the neurotransmitter, acetylcholine (ACh) is released from parasympathetic nerves and acts on muscarinic receptors on the basolateral PM. Activated muscarinic receptors promote the production of inositol 1,4,5 trisphosphate (IP_3), and subsequently Ca^{2+} release from endoplasmic reticulum (ER) stores via IP_3 receptors (IP_3Rs) situated in the ER in the extreme apical aspects of the cell (*Futatsugi et al., 2005; Lee et al., 1997; Pages et al., 2019*). Elevated $[\text{Ca}^{2+}]_i$ activates a Ca^{2+} -activated Cl^- channel named TMEM16a that allows Cl^- to move through the apical PM to the ductal lumen which is continuous with the salivary intercalated duct (*Pedersen et al., 2018; Melvin et al., 2005*). In turn, Na^+ moves through the paracellular space to balance the Cl^- and water follows osmotically both paracellularly and through the water channel aquaporin5 (AQP5) to generate the primary saliva (*Melvin et al., 2005*).

The importance of saliva is underappreciated in the absence of hypofunction. Reduced salivary secretion is termed xerostomia and can result from the iatrogenic effects of drugs, as collateral damage to salivary glands following radiotherapy for malignancy in the head and neck area, and commonly in SS (*Saleh et al., 2015*). SS is a chronic autoimmune disorder, that is predominantly manifested as profound dry eye and dry mouth as ultimately the immune system targets and destroys lacrimal and salivary gland cells (*Tabbara and Vera-Cristo, 2000; Ramos-Casals et al., 2012; Mavragani and Basiaga, 2014; Brito-Zerón et al., 2016*). SS can occur independently (primary SS, pSS) or concurrently with diseases such as arthritis or lupus (secondary SS, sSS) (*Kiripolsky et al., 2017*). SS affects millions of people, predominantly females in their fourth and fifth decades of life. While treatments can alleviate symptoms, there is no cure or intervention to halt its progression. The etiology of SS remains largely unresolved, but it's believed to result from a combination of genetic, environmental, hormonal, and possibly viral factors, causing an aberrant immune response directed against the exocrine glands. The identification of SS usually is scored by the extent of salivary hypofunction, the degree of immune infiltration, evidence of damage to minor salivary glands observed following biopsy, and the presence of autoantibodies, such as anti-SSA (Ro) and Anti-SSB (La) and anti-nuclear antibody (ANA) which are classically found in SS (*Mavragani and Basiaga, 2014; Brito-Zerón et al., 2016; Jonsson et al., 2018*). Notably, however, in the early phases of SS, there is minor immune infiltration and little overt damage to exocrine tissue despite profound hypofunction. Provocatively, these data indicate that loss of secretory tissue per se is not the causative event resulting in dryness early in the disease, and further indicates that a defect in the stimulus-secretion coupling mechanism precedes glandular destruction and possibly contributes to the progression of the disease.

Over the years, numerous mouse models both genetic and 'induced' have been developed to study the pathogenesis of SS, with each exhibiting specific aspects of the human condition, including glandular dysfunction, autoantibody production, and lymphocytic infiltration (*Lee et al., 2012; Gao et al., 2020*). To investigate the early events in SS, we concentrated on an SS model induced by the activation of the stimulator of the interferon gene (STING) pathway. This is thought to mirror the molecular response to bacterial/viral infection. STING is primarily located in the ER and plays a crucial role in the innate immune response, especially against DNA viruses and intracellular bacteria. Activation of STING occurs upon sensing cytosolic DNA as a result of cell damage or from microbial origin following infection. When cytosolic DNA is detected, it is first recognized by a sensor molecule called cGAS (cyclic GMP-AMP synthase). Binding to DNA prompts cGAS to generate cGAMP (cyclic GMP-AMP), which, in turn, binds to and activates STING (*Decout et al., 2021*). Once STING is activated, it undergoes a series of transformations that ultimately result in the transcription of type I interferon genes, especially the gene encoding interferon- β (IFN- β) (*Papinska et al., 2018*). The production of type I interferons is a primary antiviral response and a significant characteristic of SS (*Papinska et al., 2018; Huijser et al., 2022*). STING can be activated pharmacologically by exposure to 5,6-Dimethyl-9

-oxo-9H-xanthene-4-acetic acid (DMXAA), which faithfully reproduces the immune response observed following physiological STING activation ([Gao et al., 2013](#); [Weiss et al., 2017](#); [Cerón et al., 2019](#)).

In this study, we investigated the early events in the initiation of SS-like disease that lead to salivary gland hypo-function using the DMXAA SS model. We first utilized *in vivo* intravital imaging to investigate any potential dysregulation of Ca²⁺ signaling in the DMXAA-induced SS mouse model. Paradoxically, the spatially averaged Ca²⁺ levels achieved following neural stimulation in mice treated with DMXAA were enhanced despite significantly reduced fluid secretion. Notably, however, the stereotypical spatial characteristics of the Ca²⁺ signal were disrupted. Downstream of the Ca²⁺ signal, the activity of the TMEM16a Ca²⁺-activated Cl channel stimulated by muscarinic secretagogues was reduced, despite no changes in the abundance or localization of the protein or absolute sensitivity to activation by Ca²⁺. The intimate localization of IP₃R and TMEM16a was, however, disrupted, contributing to the reduced activity of TMEM16a upon agonist stimulation as local peripheral coupling between channels is disrupted. Moreover, we observed disordered mitochondrial morphology, abundance, and function in the disease model. These data suggest that early in SS, reduced fluid secretion occurs because of a defect in the secretagogue activation of Cl⁻ secretion. Further significant mitochondrial dysfunction is evident, possibly as a result of the aberrant Ca²⁺ signals that may contribute to the dysregulated Ca²⁺ signals and/or progression of SS disease.

Results

Saliva secretion is attenuated in both SMG and PG in the SS mouse model

Activation of the STING pathway in mice has been established as a model for the initiation of SS. This pathway is normally activated following exposure to foreign nucleic acids and is thought to mimic exposure of cells to DNA/RNA from viruses and bacteria. Activation of this pathway in salivary glands is characterized by initiation of a type-1 interferon response, mild immune cell infiltration, and a marked loss of saliva secretion without obvious morphological damage and, therefore, mimics the early clinical manifestations of SS disease. Thus, to investigate the early cellular events in acinar cells during the initiation of SS in mice, we chose to pharmacologically activate this pathway using DMXAA, a STING pathway agonist. As described in Methods, DMXAA (or control solution) was administered on day 0 and day 21 of the experimental timeline ([Figure 1A](#)). Immunofluorescent staining in sliced SMG tissue indicated that STING protein was increased in SMG in the DMXAA-treated mouse on day 28, seven days after the final DMXAA administration ([Figure 1—figure supplement 1](#)) confirming the activation of the STING pathway. Whole saliva production from the major salivary glands was evaluated on day 28 following systemic stimulation with the muscarinic receptor agonist, pilocarpine. To avoid potential weight-related variations in saliva secretion, the total saliva output was normalized to the individual mouse's body weight. Notably, the average saliva production was reduced from 130.1±48.96 mg in vehicle-treated mice to 63.71±30.41 mg in DMXAA-treated mice, a reduction in saliva production of 48.97% ([Figure 1B](#)). Consequently, DMXAA treatment resulted in 51.99% saliva production compared to vehicle-treated mice ([Figure 1C](#)). Moreover, H&E staining indicated that mild immune infiltration was observed in the DMXAA-treated mice with no overt changes to the morphology of the gland ([Figure 1D](#)). The mass of the SMG was also not significantly different in DMXAA vs. vehicle-treated animals, consistent with no loss of secretory tissue ([Figure 1E](#)). Collectively, these results suggest that DMXAA-treated mice exhibit characteristics of early-stage SS and could be a useful model for investigating the pathophysiological mechanisms underlying secretory dysfunction and advancing our understanding of the disease's progression.

To further investigate the individual relative contribution of the SMG and PG to the decrease in total saliva secretion using a more physiological stimulation paradigm, we performed experiments where the nerve bundle innervating a particular gland was electrically stimulated and saliva secretion quantitated. Previous research in our lab has established the range and parameters for physiological stimulation of secretion ([Takano et al., 2021](#)). The production of saliva was significantly diminished in DMXAA-treated animals compared with vehicle controls at stimulation frequencies of 7 and 10 Hz in SMG ([Figure 1F](#)) and at 5, 7, and 10 Hz in the PG ([Figure 1G](#)). These findings confirm that activation of the STING pathway reduces the function of both SMG and PG, consistent with the diminished

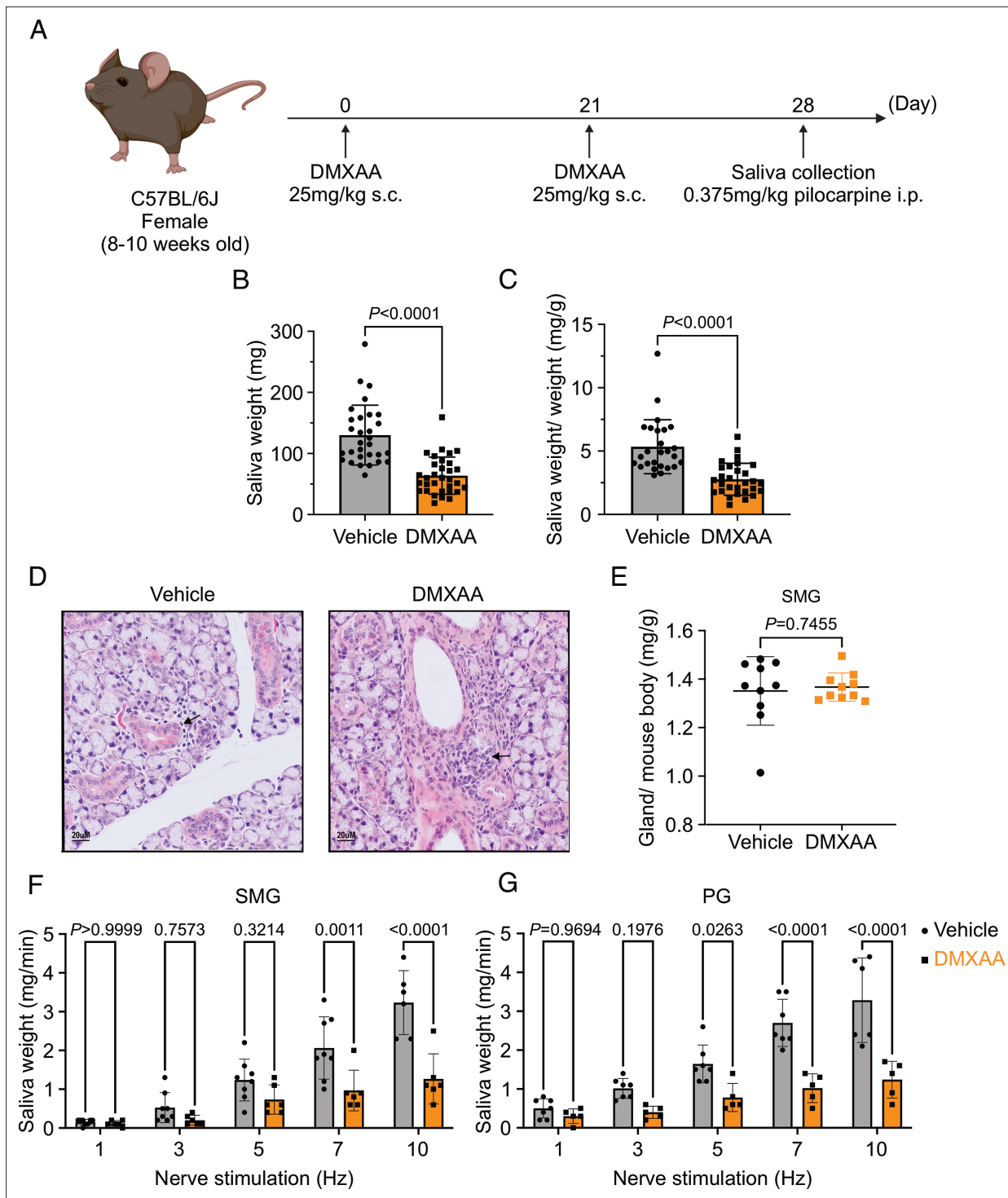


Figure 1. Deficiency in salivary secretion in 5,6-Dimethyl-9-oxo-9H-xanthene-4-acetic acid (DMXAA)-induced Sjögren's syndrome (SS) mouse model. (A) Schematic timeline for the generation of the SS mouse model. Female wild-type (WT) mice were administered two subcutaneous doses of DMXAA on Day 0 and Day 21. Salivary gland function was assessed on day 28. (B–C) Saliva, stimulated by pilocarpine, was collected over 15 min. (B) The amount of saliva secretion was determined by measuring the saliva weight. Vehicle: n=30 mice, SS mouse model: n=32 mice. Mean ± SD. (C) The weight of collected saliva was normalized to each mouse's body weight. Vehicle: n=26 mice, SS mouse model: n=29 mice. Mean ± SD. Unpaired two-tailed t-test. (D) H&E stained sections from the vehicle or DMXAA-treated animals. Treated animals showed minor lymphocyte infiltration and inflammation as focal peri-vascular/peri-ductal lymphocytic sialoadenitis adjacent to normal-looking acini. (E) The glandular damage was assessed by normalizing the weight of the submandibular gland (SMG) to the mouse's body weight. Each dot represents the weight of one SMG. n=10 from 5 mice for both vehicle-treated and DMXAA-treated mice. (F–G) A comparison of total saliva secretion following 1 min stimulations at the indicated frequency (F) from the SMG of mice

Figure 1 continued on next page

Figure 1 continued

(Vehicle: n=8 mice, SS mouse model: n=6) and (G) from the parotid gland (PG) (Vehicle: n=7 mice, SS mouse model: n=5 mice). Mean \pm SD. Two-way ANOVA with multiple comparisons. Source data is included in **Figure 1—source data 1**.

The online version of this article includes the following source data and figure supplement(s) for figure 1:

Source data 1. Raw data of amounts of salivary secretion for individual animals.

Figure supplement 1. Up-regulation of stimulator of the interferon gene (STING) protein expression in both submandibular gland (SMG) and parotid gland (PG) treated with Dimethyl-9-oxo-9H-xanthene-4-acetic acid (DMXAA).

Figure supplement 1—source data 1. Raw data for the amount of STING fluorescence per cell.

production of whole saliva. Notably, the reduction in function of PG, the gland responsible for the majority of stimulated saliva secretion, was relatively greater than in SMG.

Altered spatiotemporal characteristics of Ca²⁺ signals in the SS mouse model

An increase in intracellular Ca²⁺ plays a central role in regulating the cellular machinery underlying the fluid secretion mechanism. In particular, as noted, an increase in Ca²⁺ is important for the activation of ion channels localized in particular domains of the polarized acinar cell which play a central role in saliva secretion (Takano et al., 2021). Given that the precise spatiotemporal characteristics of the Ca²⁺ signal in salivary acinar cells are thought to be fundamental to the appropriate activation of the fluid secretion machinery, we evaluated whether hypofunction following DMXAA treatment resulted from dysregulation of the stimulated Ca²⁺ signal. Previous research in our lab developed a platform to study Ca²⁺ signaling in vivo using Multiphoton (MP) imaging in transgenic mice engineered to express a genetic-encoded Ca²⁺ indicator, GCaMP6f, specifically in acinar cells (Takano et al., 2021). These mice were generated by crossing homozygous mice expressing the fast genetically encoded Ca²⁺ indicator GCaMP6f (B6J.Cg-Gt(ROSA)26Sor^{tm95.1(CAG-GCaMP6f)Hze/MwarJ}) floxed with a STOP cassette with heterozygous tamoxifen-inducible Mist1 Cre mice (B6.129-Bhlha15^{tm3(cre/ERT2)Skz/J}). The protocol for STING pathway induction was applied to the mice expressing GCaMP6f (**Figure 2—figure supplement 1B**). Salivary gland function was assessed by the amount of pilocarpine-induced saliva secretion. The secretion deficiency observed in wild-type mice was recapitulated in these mice from a different genetic background (**Figure 2—figure supplement 1B**). We reasoned that decreased fluid secretion could result from reduced or dysregulated Ca²⁺ signaling in DMXAA-treated mice. Therefore, next, we compared the spatially averaged Ca²⁺ signal evoked by direct nerve stimulation in DMXAA-treated vs. vehicle control animals in vivo in SMG. SMG were stimulated at frequencies optimum for fluid secretion (1–10 Hz) for 10 s and the Ca²⁺ signals were recorded. **Figure 2A** shows standard deviation (SD)-projection images visualizing the spatial and amplitude changes in Ca²⁺ throughout the field of view during the entire period of stimulation at the indicated frequencies. In vehicle-treated mice, the Ca²⁺ signals at low stimulus strengths occurred in a minority of the cells and predominantly propagated below the apical PM. As the stimulation strength increased, Ca²⁺ signals became more pronounced, and more acinar cells responded. Strikingly, acinar cells in DMXAA-treated mice demonstrated enhanced sensitivity to stimulation. At lower stimulation strengths, a larger number of acinar cells responded, and the spatially averaged Ca²⁺ signals in these cells were notably larger when compared to those in the control group. **Figure 2B** shows a time series of images following 7 Hz stimulation. This augmented response was manifested as an elevated maximum peak [Ca²⁺] (**Figure 2D**), shorter latency (**Figure 2E**), and larger area under the curve (AUC) during stimulation in DMXAA-treated animals (**Figure 2F**).

In addition to the absolute magnitude of the spatially averaged Ca²⁺ signal, the subcellular spatial characteristics of the stimulated Ca²⁺ rise are also important for appropriate stimulation of fluid secretion (Takano et al., 2021). Ca²⁺ signals stimulated following nervous stimulation in SMG are invariably initiated in the extreme apical pole of acinar cells and subsequently establish a standing gradient that dissipates rapidly to result in apically confined signals that do not substantially propagate to the basal aspects of the cell following physiological stimulation (Takano et al., 2021). We, therefore, investigated if the spatial characteristics of stimulated Ca²⁺ signals were altered in DMXAA-treated animals. SD image projections generated during the period of stimulation demonstrated that the [Ca²⁺]_i increase was tightly localized below the apical PM within the acinar cells in the vehicle-treated animals

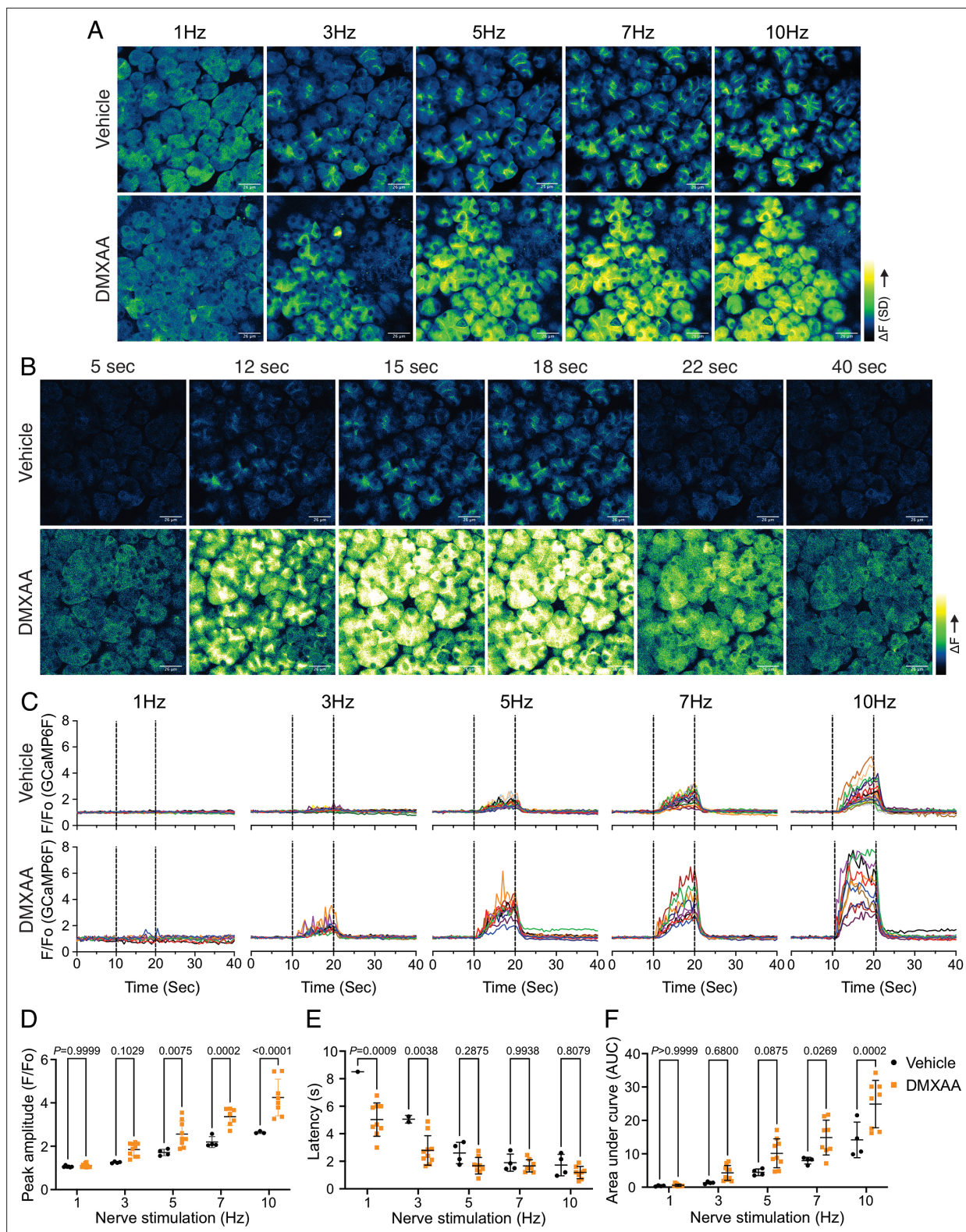


Figure 2. Augmented global Ca^{2+} signals in vivo in Sjögren's syndrome (SS) mouse model. **(A)** Representative standard deviation images of Ca^{2+} signals during the 10 s of stimulation. Scale bar: 26 μm **(B)** The time-course of pseudo-color images of Ca^{2+} in response to 7 Hz stimulation. Scale bar: 26 μm **(C)** Representative cellular responses to stimulation at the indicated frequencies averaged from the entire cell. $n=10$ cells, one animal. **(D)** A comparison of peak Ca^{2+} , **(E)** area under a curve, and **(F)** latency during each stimulation in submandibular gland (SMG). Each symbol represented the average

Figure 2 continued on next page

Figure 2 continued

response of ten cells from one view. Vehicle: n=3–6 from three mice; SS mouse model: n=8–10 from four mice. Mean ± SD. Two-way ANOVA with multiple comparisons. Source data is included in .

The online version of this article includes the following source data and figure supplement(s) for figure 2:

Source data 1. Raw data for salivary secretion from individual animals.

Figure supplement 1. Deficiency in secretion in transgenic animals expressing GCamp6f following Dimethyl-9-oxo-9H-xanthene-4-acetic acid (DMXAA) treatment.

Figure supplement 1—source data 1. Raw data for the amount of saliva secretion for individual animals.

(**Figure 3A**). However, in the DMXAA-treated animals, the $[Ca^{2+}]_i$ exhibited a more global distribution through the entire cell cytoplasm (**Figure 3B**). The $[Ca^{2+}]_i$ was visualized via line-scan plots revealing the temporal alterations along a line extending from the apical PM to the basolateral PM, traversing the nucleus, over time within an acinar cell. A significant $[Ca^{2+}]_i$ elevation was evident at the basolateral aspects of the acinar cell in the DMXAA-treated animals (**Figure 3D**) when compared to the vehicle-treated control (**Figure 3C**). As shown in the kinetic plots, the $[Ca^{2+}]_i$ in the apical region is greater in DMXAA-treated mice compared to the vehicle-treated mice (**Figure 3E**). Moreover, a significant Ca^{2+} signal was observed in the extreme basal region of the cell in DMXAA but not in vehicle-treated animals (**Figure 3F**). The comparison of Ca^{2+} signal ratios at the apical versus basolateral PM indicated the most significant globalization of the Ca^{2+} signal occurred at 10 Hz stimulation (**Figure 3G**) which corresponds to the stimulation strength that results in maximal fluid secretion (*Takano et al., 2021*). In total, these data demonstrate that the magnitude of the spatially averaged Ca^{2+} signal, together with the spatiotemporal characteristics of the signal are altered in the DMXAA-treated animals, but that these changes can not readily account for the reduction in fluid secretion observed.

Secretagogue-stimulated TMEM16a activity is suppressed in the SS mouse model

The rate-limiting step for the secretion of fluid is the activation of the Ca^{2+} -activated Cl^- channel, TMEM16a. We considered that a reduction in fluid secretion could conceptually occur by a reduction or mislocalization of TMEM16a protein, or by compromised muscarinic receptor-stimulated activation of the channel. Western blotting indicated the TMEM16a protein expression was comparable between the vehicle and SS mouse models (**Figure 4A and B**). In addition, immunolocalization using confocal microscopy demonstrated that TMEM16a localization remained largely unchanged in the SS mouse model (**Figure 4C**). Thus, a decrease in protein expression or mislocalization of the protein does not result in a reduction in stimulated saliva secretion. Similarly, the expression and localization of Aquaporin 5 were also not altered (**Figure 4—figure supplement 1A–C**). We next investigated whether the activation of this ion channel was compromised in DMXAA-treated animals using whole-cell patch clamp electrophysiology. In the absence of stimulation, no Cl^- currents were observed in either vehicle or DMXAA animals following either depolarizing or hyperpolarizing voltage steps from a holding potential of -50 mV (**Figure 4D**). In the presence of 1 μ M of the muscarinic agonist Carbachol (CCh), robust Cl^- currents were measured in acini prepared from vehicle-treated animals (**Figure 4E**), which were greatly reduced in DMXAA-treated animals (**Figure 4D and F**). Reduced CCh-stimulated Cl^- currents could potentially occur because of altered Ca^{2+} regulation of TMEM16a following disruption of the spatial characteristics of the stimulated Ca^{2+} signal. Theoretically, it is also possible that the $[Ca^{2+}]_i$ in the immediate vicinity of TMEM16a was disrupted, despite the augmented spatially averaged peak response. We, therefore, next tested whether TMEM16a activity stimulated directly by 0.5 , 1 or 5 μ M Ca^{2+} in the pipette solution (and thus globally in the cytoplasm) was altered in DMXAA-treated animals. Surprisingly, TMEM16a was activated to a similar extent by Ca^{2+} in the SS mouse model (**Figure 5A and B**). In total, our data suggest that TMEM16a abundance, localization, or activity per se are not altered and thus do not explain the significant reduction in saliva secretion in the DMXAA-treated model.

An alternative mechanism could be that the microdomain between the apical ER Ca^{2+} release sites and the apical PM TMEM16a is disrupted in the disease model, resulting in compromised local coupling between the ER and PM channels. Therefore, we investigated how the activation of TMEM16a was affected by buffering the CCh-stimulated cytosolic Ca^{2+} with slow and fast Ca^{2+} chelators. EGTA is a

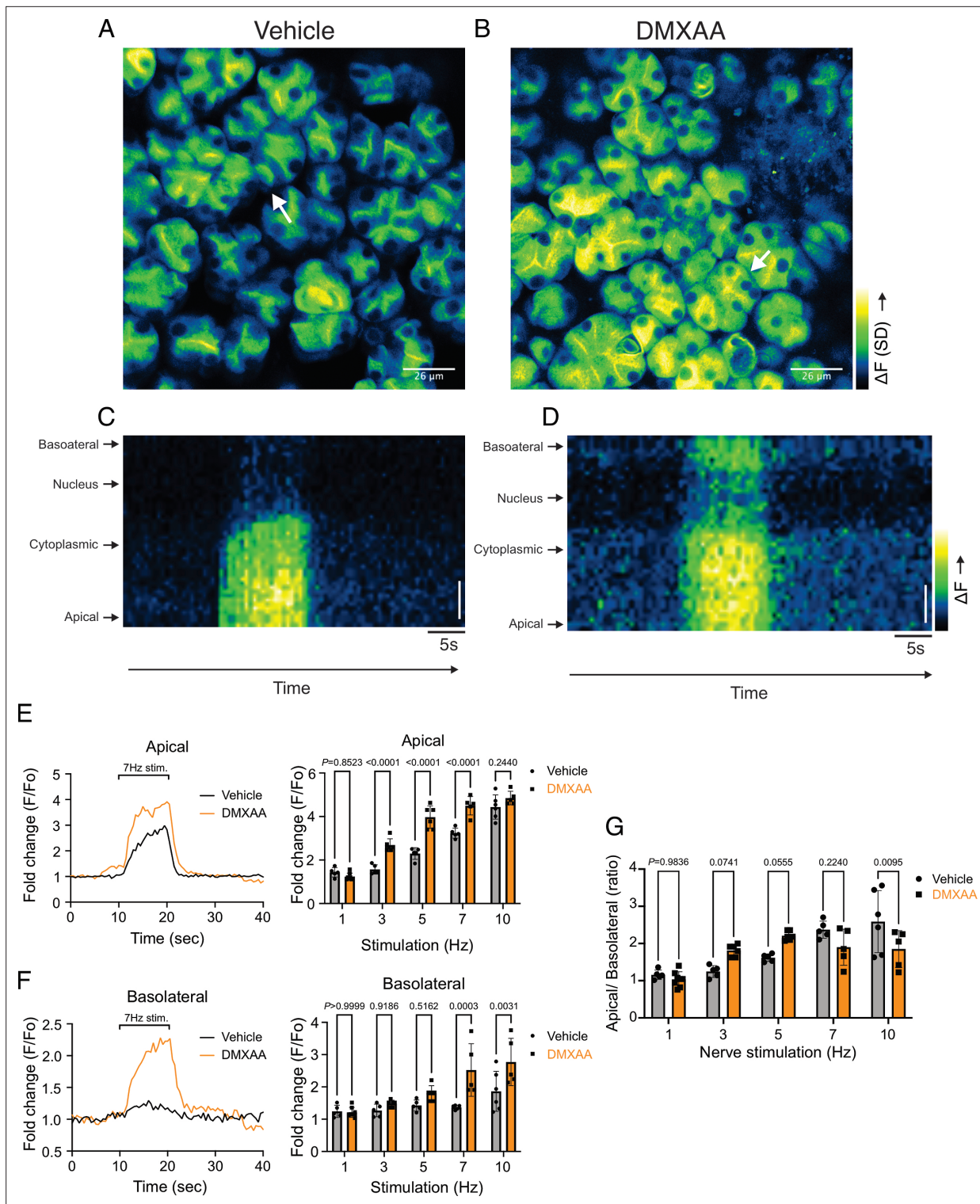


Figure 3. Disrupted spatial localization of Ca²⁺ signals in vivo in Sjögren's syndrome (SS) mouse model. **(A–B)** A representative standard deviation image during the 7 Hz stimulation in **(A)** vehicle condition and **(B)** in the SS mouse model. Scale bar: 26 μm. An acinus is outlined by the white broken line and a line from apical to basal is shown in red in each standard deviation (SD) image. **(C–D)** A representative 'kymograph' image of consecutive lines stacked in space over time for 7 Hz stimulation in **(C)** vehicle condition and **(D)** SS mouse model. Time is encoded along the X-axis from left to right. Space is encoded along the Y-axis from the apical side (bottom) to the basolateral side (top). Scale bar: 3 μm. **(E)** Representative trace of Ca²⁺ signals at 7 Hz nerve stimulation in an apical ROI generated as the initial 2 mm of the scanned line over time (yellow line) in vehicle-treated (black) and DMXAA-treated (orange) mice. The changes in apical ROI fluorescence at the indicated frequencies were quantified as the maximal Ca²⁺ changes normalized

Figure 3 continued on next page

Figure 3 continued

to the basal intensity. (F) Representative trace of Ca^{2+} signals following 7 Hz nerve stimulation in a basolateral ROI generated as the final 2 mm of the scanned line (yellow line) over time in vehicle-treated (black) and DMXAA-treated (orange) mice. The changes in basolateral Ca^{2+} signals at the indicated frequencies were quantified by the maximal Ca^{2+} changes normalized to the basal intensity. (G) The ratio of the magnitude of Ca^{2+} signal on the apical vs. the basolateral ROI upon stimulation at the indicated frequencies. Vehicle: n=5–6 replicates from three mice; SS mouse model: n=5–8 replicates from four mice. Mean \pm SD. Two-way ANOVA with multiple comparisons. Source data is included in **Figure 3—source data 1**.

The online version of this article includes the following source data for figure 3:

Source data 1. Raw data for individual animals.

high-affinity Ca^{2+} buffer with slow kinetics, while BAPTA has much more rapid kinetics. Experimentally, BAPTA can quickly buffer Ca^{2+} changes close to Ca^{2+} release sites and limit local activation of effectors within 20 nm. In contrast, EGTA has been shown to attenuate the rise in the bulk cytosol but is too slow to buffer local Ca^{2+} in a restricted microdomain (Eisner et al., 2023). In the presence of BAPTA, no Cl^- currents were detected in either vehicle-treated or DMXAA-treated animals (Figure 6A). However, in the presence of the slow Ca^{2+} chelator, EGTA, CCH-stimulated Cl^- currents were observed in acinar cells from vehicle-treated animals but were absent in the DMXAA-treated animals (Figure 6A and B). These data suggest that physiologically TMEM16a is activated by local changes in Ca^{2+} signaling as a result of IP_3 -induced Ca^{2+} release in the apical domain of the acinar cell.

We noted that the abundance of $\text{IP}_3\text{R}2/3$ was not significantly altered in DMXAA-treated animals (Figure 7—figure supplement 1A–C), nevertheless next, we employed STED super-resolution microscopy to closely examine the spatial relationship between apical PM TMEM16a and $\text{IP}_3\text{R}3$ on the apical ER (Figure 7A). Despite the cell-cell contact distance remaining consistent in the disease model, as indicated by the distance between TMEM16a on the PM of adjacent acinar cells (Figure 7F), a notable increase in distance between the apical TMEM16a and $\text{IP}_3\text{R}3$ expressed on apical ER compared to the control group was observed (Figure 7E). In the control mice, the distance between TMEM16a and $\text{IP}_3\text{R}3$ was on average 84 ± 17 nm, versus 155 ± 20 nm in the SS disease mice. Similarly, the distance between $\text{IP}_3\text{R}3$ in adjacent cells was increased from 505 ± 34 nm to 689 ± 68 nm (Figure 7C and D). In total, these observations support the conclusion that the reduced activity of the TMEM16a channel is attributable to the disruption of the microdomain between TMEM16a and $\text{IP}_3\text{R}3$, such that the Ca^{2+} flux through the IP_3R is not communicated appropriately to its effector, TMEM16a.

Compromised mitochondrial morphology and metabolism in the SS mouse model

Ca^{2+} modulates cellular metabolism by the intricate bidirectional interaction between the ER and mitochondria. Ca^{2+} transfer between ER and mitochondria is essential for optimal bioenergetics, and dysregulated $[\text{Ca}^{2+}]_i$ can be deleterious to mitochondrial function and alter morphology (Duchen, 2000; Csordás et al., 2006; Ye et al., 2021; Katona et al., 2022). The transfer of Ca^{2+} between ER and mitochondria is dependent on the intimate physical localization of the organelles (Katona et al., 2022). Notably, aberrant mitochondrial morphology has been reported in the salivary glands of SS patients (Barrera et al., 2021). We first investigated mitochondrial abundance and morphology by immunofluorescence staining with antibodies directed against ATP5A, a component of the ATP synthesis machinery to visualize mitochondria, and Na^+/K^+ ATPase to localize the plasma membrane (Figure 8A). Using previously published methodologies (Valente et al., 2017; Harwig et al., 2018), quantification revealed a $22.16\%\pm 4.95$ reduction in mitochondrial numbers in the SS mouse model relative to the vehicle-treated control (Figure 8B). Consistent with reduced mitochondrial numbers, less area was occupied by mitochondria in DMXAA-treated acinar cells (Figure 8C). Mitochondria morphology is intricately linked to their bioenergetic status. We next evaluated mitochondrial morphology by their 'so-called' aspect ratio (AR) and form factor (FF) in DMXAA and vehicle-treated animals. The AR, the length of the major over minor axes of mitochondria documents the degree of fragmentation or elongation of individual mitochondria (Katona et al., 2022; Harwig et al., 2018). Mitochondria exhibited an $18.35\%\pm 4.62$ decrease in mitochondrial elongation (Figure 8D) and a $20.7\%\pm 7.78$ decrease in mitochondrial branching (Figure 7E) in the disease model compared to the vehicle-treated control condition. Importantly, these changes in mitochondrial number and morphology were not exclusive to the SMG as similar patterns were observed in the PG mitochondria,

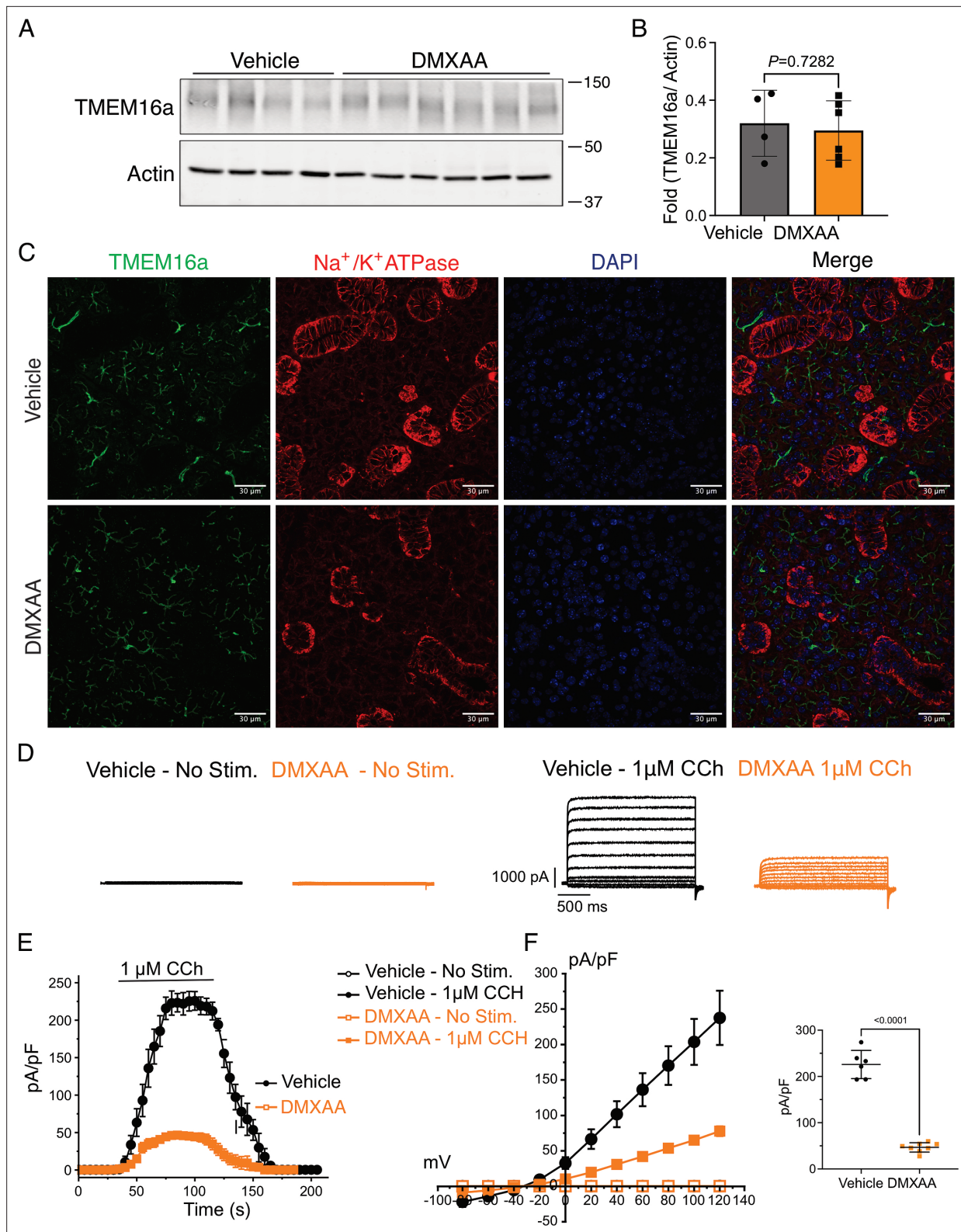


Figure 4. Attenuated whole-cell macroscopic Cl^- currents induced by Carbachol (CCh) stimulation in Sjögren's syndrome (SS) mouse model. **(A)** Western blotting showing the protein expression level of TMEM16a in the vehicle condition and the 5,6-Dimethyl-9-oxo-9H-xanthine-4-acetic acid (DMXAA)-treated SS mouse model. Actin is the internal control. **(B)** The quantification of TMEM16a protein expression normalized to the internal control, Actin. Vehicle, $n=4$ mice; SS mouse model: $n=6$ mice. **(C)** Immunofluorescent staining in submandibular gland (SMG) tissue for TMEM16a (green), Na^+/K^+ ATPase (red), and DAPI for nucleus (blue). The upper panel is from the vehicle-treated control and the bottom panel is from DMXAA-

Figure 4 continued on next page

Figure 4 continued

treated animals. Scale bar: 30 μm . Unpaired two-tailed t-test. (D) Cl^- currents when cells were held at -50 mV and stepped from -80 – 120 mV in 20 mV increments. (E) Time-dependent Cl^- current density changes in response to the Carbachol (CCh) in the isolated acinar cells in vehicle conditions and SS mouse model. (F) Current-voltage relationships were measured before and after the addition of CCh in vehicle conditions ($n=$ three mice, 3–4 cells per mouse) and SS mouse model ($n=$ three mice, 3–4 cells per mouse). TMEM16a currents in the treated mice were markedly reduced compared to the control mice. Black dots represent the vehicle-treated cells and orange squares represent DMXAA-treated cells. The open symbols represent no stimulation; the solid symbols represent CCh stimulation. Source data is included in **Figure 4—source data 1 and 2**.

The online version of this article includes the following source data and figure supplement(s) for figure 4:

Source data 1. Raw densitometry and current magnitude data.

Source data 2. Original immunoblots.

Figure supplement 1. Aquaporin5 (AQP5), the water channel, remained the comparable expression and proper localization in submandibular gland (SMG) in the disease mouse model.

Figure supplement 1—source data 1. Raw densitometry data.

Figure supplement 1—source data 2. Original immunoblots.

again marked by reduced mitochondrial count, increased fragmentation, and decreased branching (**Figure 8—figure supplement 1A–E**).

Next, we utilized electron microscopy (EM) to investigate mitochondrial ultrastructure. At low magnification, acinar cells from control mice contained defined mitochondria and well-formed ER stacks (**Figure 9A**, blue arrow). In contrast, the ER structure was disrupted in the SS disease model (**Figure 9A'**). At higher magnification, the coordinated ER structure was largely absent in diseased mice (**Figure 9B and B'**), and the proximity between ER and mitochondria was disrupted (**Figure 9H and I**). Moreover, we also observed scattered mitochondrial cristae at the highest magnification (**Figure 9C', and G**). Consistent with immunofluorescence studies, quantification of EM micrographs revealed that mitochondria were smaller, more fragmented (**Figure 9D and E**), and rounder (**Figure 9F**) in shape. In summary, our results collectively indicate significant morphological alterations in mitochondria in the SS disease model.

Mitochondrial morphology is a dynamic process that is intimately associated with mitochondrial bioenergetics and alterations in both, occur in response to changes in cellular status (**Hogan et al., 2005; Martínez et al., 2020; Navaratnarajah et al., 2021; Schaefer et al., 2019; Zorova et al., 2018**). Therefore, we investigated if changes in morphology might be associated with the disrupted function of mitochondria in the disease model. We measured mitochondrial membrane potential ($\Delta\Psi_m$), established by the electrochemical H^+ gradient, which is the driving force of ATP production. Isolated SMG

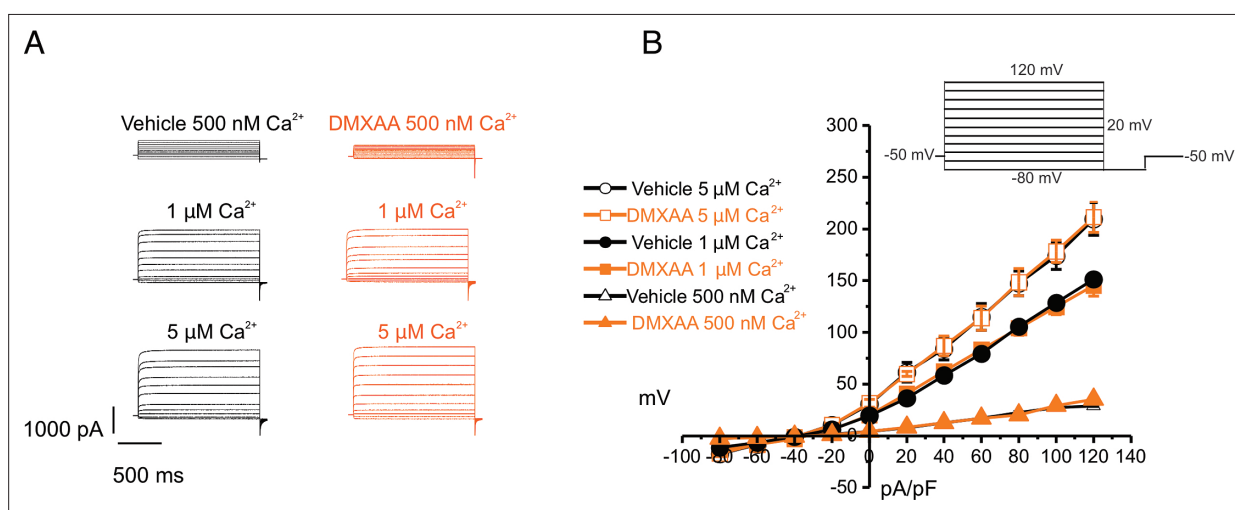


Figure 5. Increased $[\text{Ca}^{2+}]_i$ is capable of restoring TMEM16a functionality to 5,6-Dimethyl-9-oxo-9H-xanthene-4-acetic acid (DMXAA)-treated mice. (A) Cl^- currents when cells were held at -50 mV and stepped from -80 – 120 mV in 20 mV increments. Either 0.5, 1, or 5 μM $[\text{Ca}^{2+}]_i$ in the patch pipette elicited a similar magnitude of Cl^- currents for both the treated ($n=3$ mice, 3–4 cells per mouse) and control mice ($n=3$ mice, 3–4 cells per mouse). (B) Current-voltage relationships for both populations were essentially identical. Vehicle and SS mouse model: $n=3$ mice, 3–4 cells per mouse.

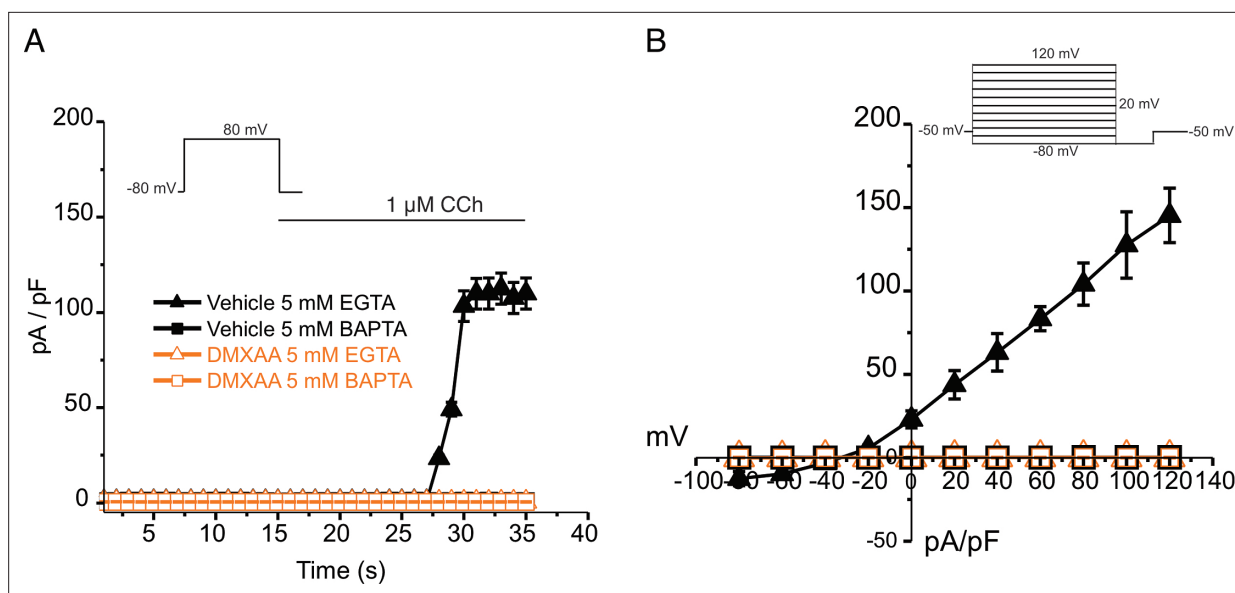


Figure 6. EGTA abolishes TMEM16a currents in 5,6-Dimethyl-9-oxo-9H-xanthene-4-acetic acid (DMXAA)-treated mice. **(A)** Cl^- currents in cells held at -80 mV and stepped to 80 mV with Carbachol (CCh) addition in EGTA (slow) and BAPTA (fast) buffered cells, respectively. **(B)** Current-voltage relationships were measured after the addition of CCh in 5 mM EGTA and 5 mM BAPTA-loaded isolated acinar cells from vehicle conditions ($N=3$ mice, $3-4$ cells per mouse) and Sjögren's syndrome (SS) mouse model ($n=3$ mice, $3-4$ cells per mouse). No TMEM16a currents in acini in either vehicle or DMXAA-treated mice in cells buffered with BAPTA. Triangles represent the 5 mM EGTA condition; squares represent the 5 mM BAPTA condition. The solid black symbols represent the vehicle-treated cells and hollow orange symbols represent DMXAA-treated cells.

acinar cells were loaded with TMRE, a $\Delta\Psi_m$ -specific dye, and MitoTracker Green, to confirm mitochondrial localization and to facilitate the normalization of indicator loading. The maximal z-stacks projection images taken by confocal microscopy revealed colocalization of TMRE with MitoTracker Green (**Figure 10A**). The basal TMRE fluorescence was reduced in cells from DMXAA vs. vehicle-treated animals (**Figure 10—figure supplement 1**). To assess $\Delta\Psi_m$, we quantified the relative maximum dissipation of $\Delta\Psi_m$ in DMXAA and vehicle-treated acinar cells by the mitochondrial uncoupler, FCCP (**Figure 10B**). Consistent with the reduction in basal TMRE fluorescence, the change in TMRE fluorescence normalized to mitochondrial content revealed a marked reduction in $\Delta\Psi_m$ in the acinar cells from the SS disease model (**Figure 10C**).

An appropriate $\Delta\Psi_m$ mitochondrial membrane potential is vital for maintaining bioenergetics (Zorova et al., 2018). Given that mitochondrial $\Delta\Psi_m$ was significantly depolarized in DMXAA-treated animals, we next evaluated the OCR, a key metric of mitochondrial bioenergetic function in isolated SMG acinar cells. We employed sequential exposure to agents that target the function of the mitochondrial electron transport chain (ETC) using Seahorse technology (**Figure 10D**). Our results revealed a 25% reduction in basal OCR in the SS model compared to the control animals (at -25.25 ± 7.89 pmol/min; **Figure 10E**). While ATP-linked respiration showed no significant difference in post-oligomycin-induced ETC Complex V blockade in both conditions (**Figure 10F**). Intriguingly, the FCCP-provoked maximal respiration rate, an indicator of stress tolerance, remarkably declined by $47\% \pm 9.19$ after FCCP treatment in the SS model (**Figure 10G**). These data indicate impaired mitochondrial function and stress responses in the SS mouse model.

Discussion

SS is a complex inflammatory disease resulting from the intersection of genetics and environmental factors. This autoimmune disorder affects exocrine glands including salivary and lacrimal glands, leading to dry mouth and dry eyes, among other symptoms (Ramos-Casals et al., 2012; Mavragani and Basiaga, 2014; Brito-Zerón et al., 2016). SS animal models are crucial for understanding the pathogenesis, progression, and potential treatments for the disease, though like many animal models of disease, none can recapitulate all the aspects of SS. Currently, SS animal models are categorized

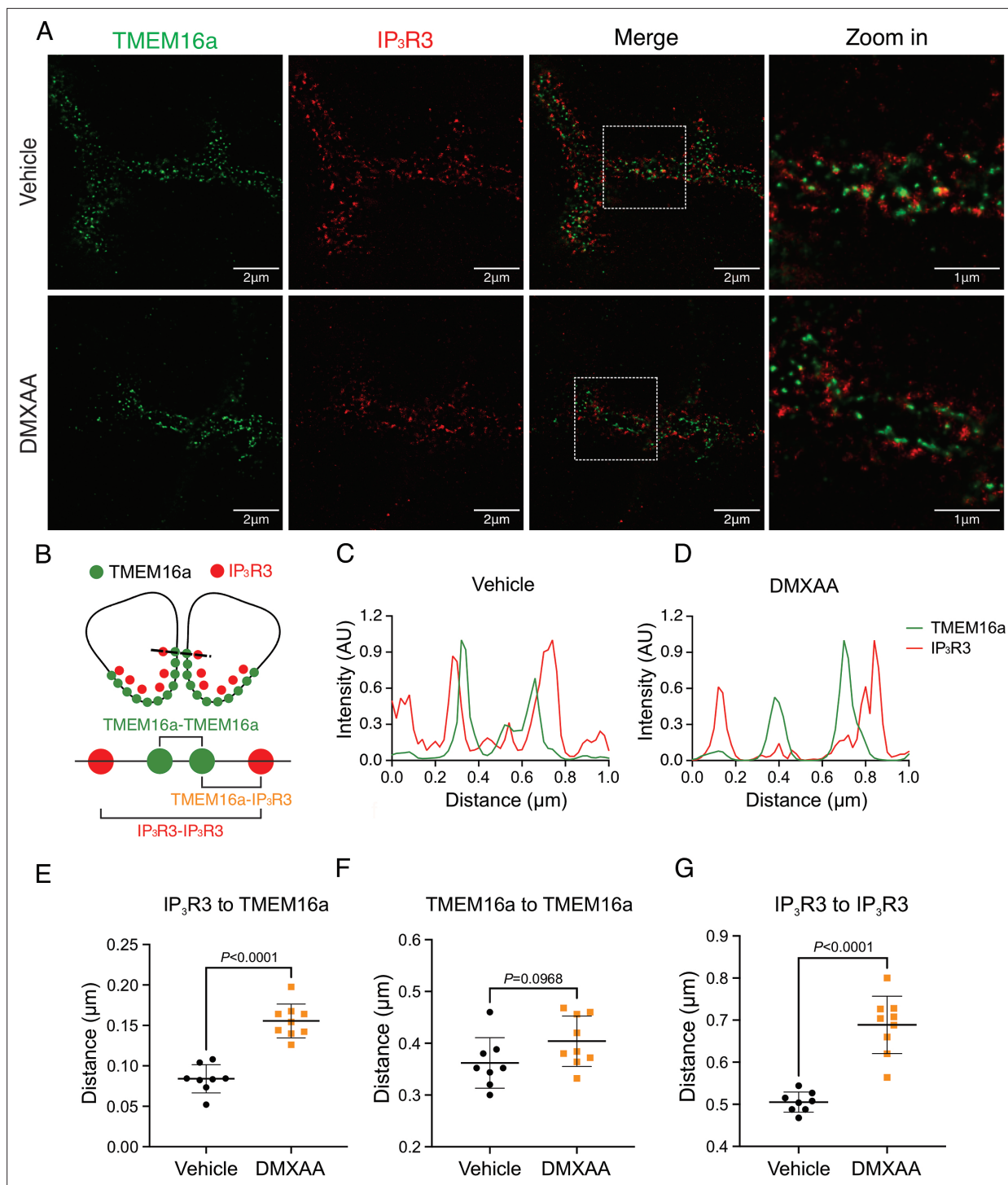


Figure 7. Disrupted proximity between TMEM16a and IP₃R3 in the 5,6-Dimethyl-9-oxo-9H-xanthene-4-acetic acid (DMXAA)-treated Sjögren's syndrome (SS) mouse model. **(A)** Maximum projection of a STED z stack (1 μm) showing TMEM16a (green) and IP₃R3 (red) in submandibular gland (SMG) tissue following Huygens deconvolution. The top panel represents the vehicle-treated control, and the bottom panel represents the SS mouse model. Scale bar: 2 μm. Zoomed images highlight the localization of TMEM16a and IP₃R3 from the white square on the merged images. **(B)** Diagram illustrating the positioning of apical PM TMEM16a and apical IP₃R3 in acinar cells. To analyze the proximity, a 1 μm reference line was drawn across the two parallel TMEM16a over two adjacent acinar cells with IP₃R3 aligned vertically in the cytoplasm. **(C–D)** The representative traces of changes in fluorescence of TMEM16a (green) and IP₃R3 (red) over the 1 μm distance. **(E)** Analysis of distance between TMEM16a and IP₃R3 within cells. **(F)** Analysis of the distance between parallel TMEM16a on adjacent acinar cells. **(G)** Distance measurement of apical IP₃R3 between two cells. Each symbol represents the mean of *Figure 7 continued on next page*

Figure 7 continued

5 examinations per image. Vehicle: n=8 replicates from 3 mice; SS mouse model: n=9 replicates from 3 mice. Mean \pm SD. Unpaired two-tailed t-test. Source data is included in **Figure 7—source data 1**.

The online version of this article includes the following source data and figure supplement(s) for figure 7:

Source data 1. Raw distance measurements for individual line profiles.

Figure supplement 1. No significant alteration in IP₃R protein levels in submandibular gland (SMG) in the 5,6-Dimethyl-9-oxo-9H-xanthene-4-acetic acid (DMXAA)-treated mouse model.

Figure supplement 1—source data 1. Raw densitometry data.

Figure supplement 1—source data 2. Original immunoblots.

as either those derived from genetically modified mice (Kiripolsky et al., 2017; Yanfei Hu et al., 1992; Shen et al., 2006; Shen et al., 2009) or those where disease is induced by specific agents or environmental factors. In the context of SS, DMXAA-induced SS can be used to mimic the early stages of the disease which might be triggered in response to bacterial or viral infection. This model is particularly effective in simulating type-1 interferon immune responses seen in early SS, which is thought to contribute to the initial glandular inflammation (Tabbara and Vera-Cristo, 2000; Papinska et al., 2018; Papinska et al., 2020). It should also be noted that DMXAA also has been reported to inhibit NAD(P)H quinone oxidoreductase (Phillips, 1999) and thus the potential increase in free radical load in cells could contribute to the phenotype. The rapid symptom manifestation of disease in the DMXAA-induced model offers an advantage for investigating the early development of SS disease since DMXAA induction is a temporally controlled process, allowing the precise staging of disease onset, thus facilitating studies on the initiating events and ultimately potential early intervention and prevention strategies.

Our studies investigated stimulus-secretion coupling when fluid secretion from SMG and PG in response to physiological stimulation was significantly reduced. Previous work has established a crucial link between an increase in $[Ca^{2+}]_i$ and stimulation of fluid secretion in the salivary glands (Melvin et al., 2005; Takano et al., 2021). Efficient secretion is reliant on the specific spatiotemporal regulation of secretagogue-stimulated $[Ca^{2+}]_i$ signals. Given this idea, our initial hypothesis was that a deficiency in secretion after DMXAA administration could be due to reduced or disrupted secretagogue-stimulated $[Ca^{2+}]_i$ signals. Indeed, previous work has revealed that in human SS patient acinar cells and the IL14 α knock-in transgenic SS mouse model, CCh-induced $[Ca^{2+}]_i$ signals were diminished. This reduction was attributed to lower expression levels of the IP₃R2 and IP₃R3 proteins (Teos et al., 2015). To probe this hypothesis, we employed transgenic animals that express the fast Ca^{2+} indicator-GCaMP6f specifically in the acinar cells. Firstly, we validated that the activation of the STING pathway leads to similar salivary gland hypofunction in this genetic background. Surprisingly, DMXAA treatment led to a striking increase in the magnitude of neurally-induced spatially averaged $[Ca^{2+}]_i$ signals. This observation is not consistent with the loss of IP₃R proteins being responsible for reduced fluid secretion previously reported in other SS models. Indeed, the expression of IP₃R proteins was unchanged following DMXAA treatment. The discrepancy could be attributed to the stage of SS disease represented by the previous studies, with our data presenting an earlier initiating phase of SS disease prior to progression, at a time point before any notable decrease in IP₃R proteins has occurred. The molecular mechanism responsible for augmented global Ca^{2+} signals following DMXAA treatment requires further study. Increased Ca^{2+} release/influx, or conversely reduced Ca^{2+} clearance might be responsible. It is tempting to speculate that reduced mitochondrial Ca^{2+} uptake and/or reduced PMCA and SERCA activity as a result of decreased ATP levels may contribute to enhanced cytosolic signals. Nevertheless, we suggest that the augmented Ca^{2+} signals might represent a compensatory mechanism to drive fluid secretion in the face of compromised physiological stimulus-secretion coupling. Although the Ca^{2+} signals were not reduced, the spatiotemporal characteristics of the Ca^{2+} signal were markedly disrupted. Specifically, during neural stimulation, while in control animals there is a pronounced standing gradient of $[Ca^{2+}]_i$ such that the $[Ca^{2+}]_i$ is much greater in the apical vs. basal aspects of the cell, in DMXAA-treated animals this gradient is largely absent as large changes in Ca^{2+} are propagated to the basal regions of the cells. It is conceivable that the alteration in magnitude coupled with changes in the spatial characteristics of the Ca^{2+} signal contributes to

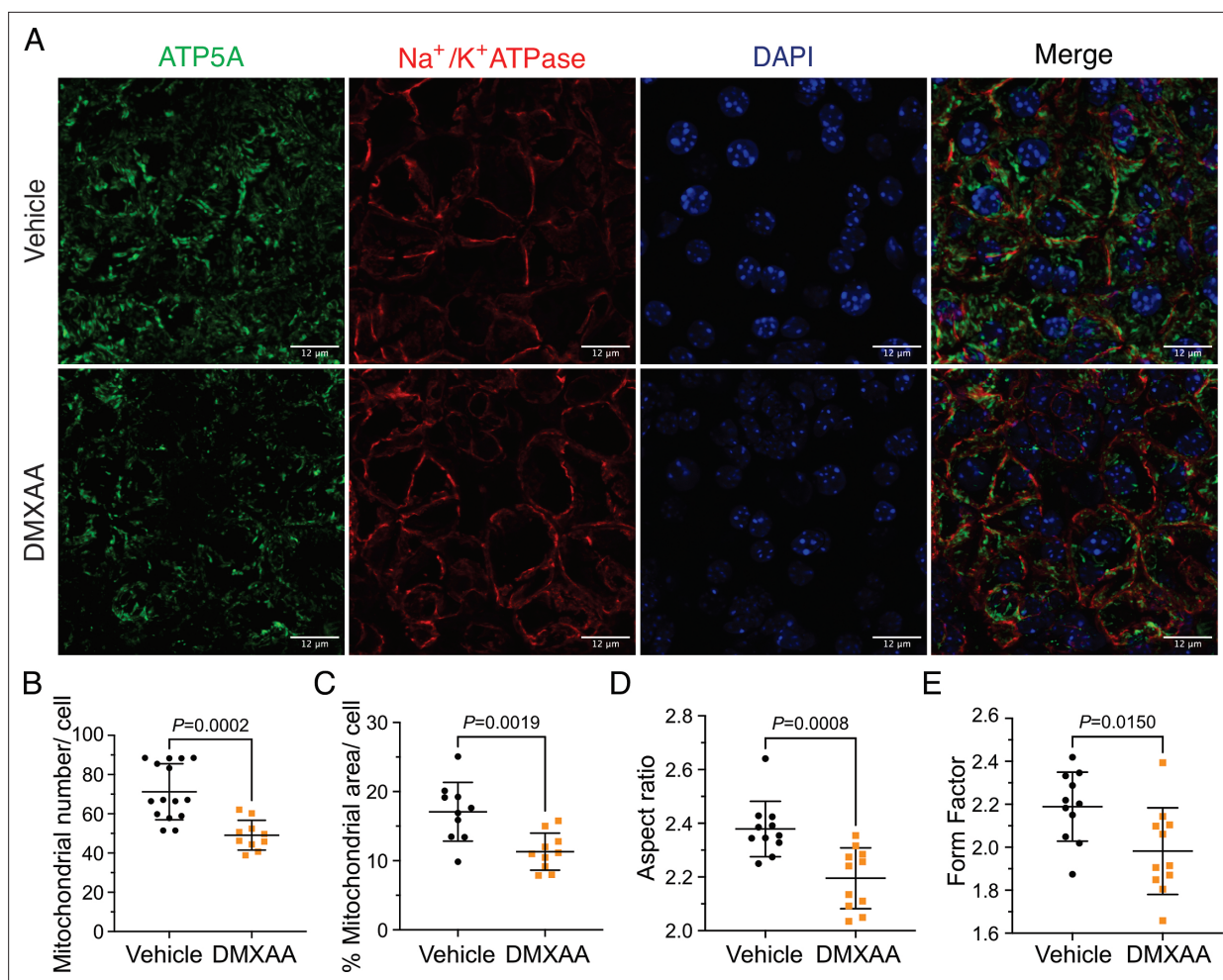


Figure 8. Mitochondrial alterations in acinar cells from the 5,6-Dimethyl-9-oxo-9H-xanthine-4-acetic acid (DMXAA)-treated Sjögren's syndrome (SS) mouse model. **(A)** Immunofluorescent staining in submandibular gland (SMG) tissue for ATP5A (green), Na⁺/K⁺ ATPase (red), and DAPI for nucleus (blue). The upper panel is the vehicle, and the bottom panel is the SS mouse model. Scale bar: 12 μ m. The mitochondrial content was quantified by **(B)** the mitochondrial number per acinar cell and **(C)** the percentage of area occupied by mitochondria per acinar cell. The mitochondrial morphology was analyzed by the **(D)** aspect ratio (AR) for the degree of mitochondrial tubular shape and **(E)** form factor (FF) for the degree of mitochondrial branching (complexity). In **(B)** to **(E)**, black dots represent the vehicle condition, and orange squares indicate the SS mouse model. Each symbol represents the mean of 10 cells per image. Vehicle: n=10–15 from 3 mice; SS mouse model: n=10–11 from 3 mice. Mean \pm SD. Unpaired two-tailed t-test. Source data is included in **Figure 8—source data 1**.

The online version of this article includes the following source data and figure supplement(s) for figure 8:

Source data 1. Raw mitochondrial morphology data.

Figure supplement 1. Mitochondrial alterations in the parotid gland of Sjögren's syndrome (SS) mouse model.

Figure supplement 1—source data 1. Raw mitochondrial morphology data.

both the defect in fluid secretion and downstream cellular changes including mitochondrial damage to ultimately result in the progression of disease.

We investigated whether changes in the secretory machinery per se were altered in DMXAA-treated animals to result in hyposalivation. Salivary gland fluid secretion is dependent on TMEM16a facilitating Cl⁻ flux across the apical PM as the driving force for water transport paracellularly and through AQP5 (Jin et al., 2016; Romanenko et al., 2010). The loss of either TMEM16a or AQP5 results in markedly attenuated fluid secretion (Romanenko et al., 2010; Tsubota et al., 2001; Catalán et al., 2015; Zeng et al., 2017). These findings indicate that alteration in expression level, localization, or regulation of these channels could potentially impact fluid secretion. Notably, in DMXAA-treated mice, the AQP5 expression and localization remain unchanged, consistent with a study in human labial

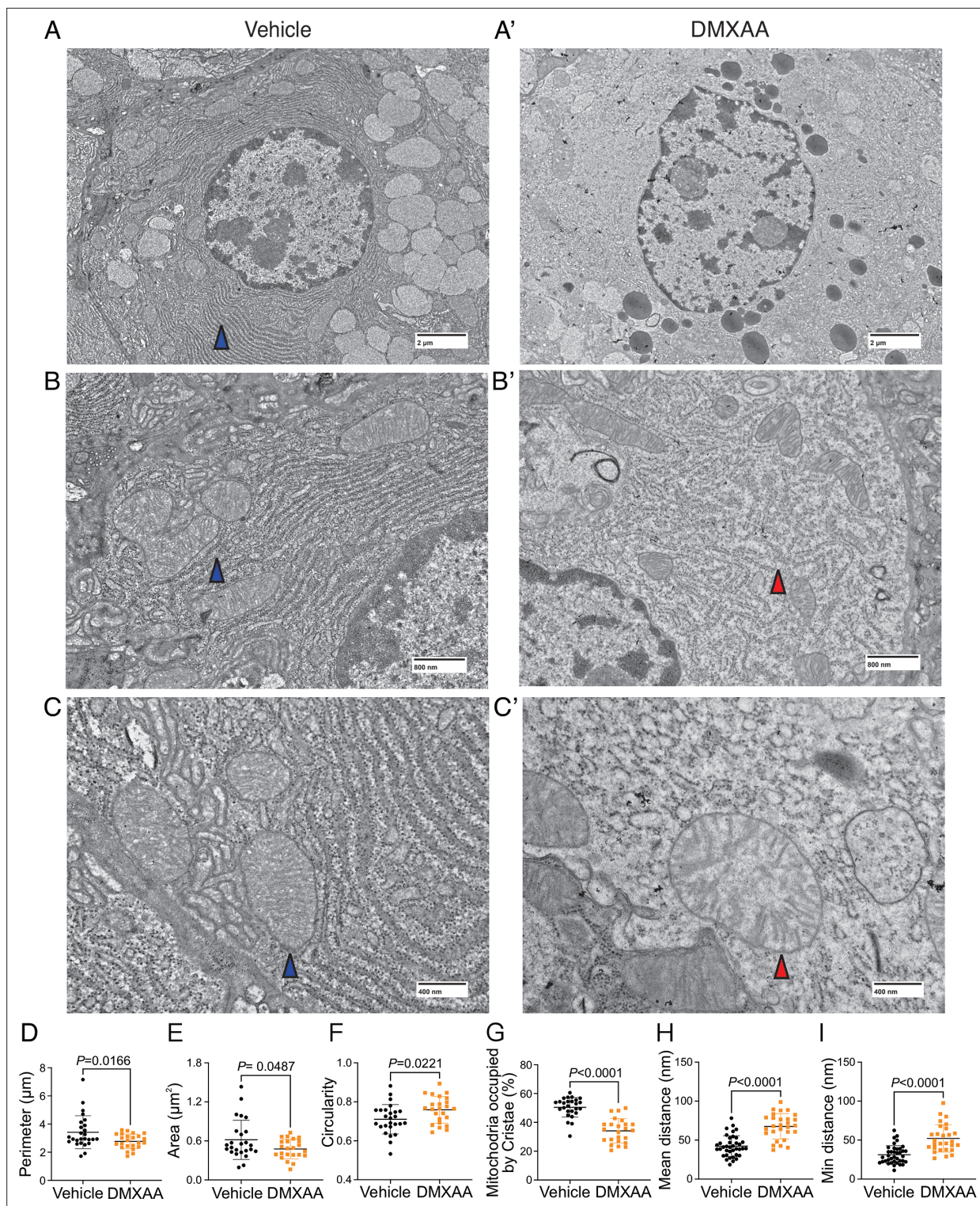


Figure 9. Ultrastructural analysis of mitochondria and endoplasmic reticulum (ER) in Sjögren's syndrome (SS) mouse model. (A-C') Images show mitochondrial cristae and ER structure by an electron microscopy (EM) at scales of (A-A') 2 μm, (B-B') 800 nm, and (C-C') 400 nm. (D) Mitochondrial perimeter, (E) mitochondrial area, and (F) circularity were quantified by the shape description in ImageJ. (G) Quantification of mitochondrial cristae dispersion was evaluated by the percentage of cristae occupied in one mitochondrion. The (H) mean and (I) minimum proximity of ER and mitochondria were quantified by the plugin from <http://sites.imagej.net/MitoCare/> in ImageJ. Vehicle: n=38 and SS mouse model: n=36 from 3 mice. Mean ± SD. Unpaired two-tailed t-test. Source data is included in **Figure 9—source data 1**.

The online version of this article includes the following source data for figure 9:

Figure 9 continued on next page

Figure 9 continued

Source data 1. Raw mitochondrial morphology data.

minor salivary glands (Gresz et al., 2015). We next examined whether the TMEM16a channel function was compromised in the model. Our electrophysiological analysis revealed a significant decrease in TMEM16a activity following CCh-induced stimulation. Again, this reduced activity was not the result of overt mislocalization or lower expression levels of the protein (Figure 4A and C). Interestingly, although the secretagogue-stimulated TMEM16a was reduced in acinar cells from DMXAA-treated animals, the sensitivity of the channel to direct activation by Ca^{2+} in the patch pipette appeared unaffected. IP_3R Ca^{2+} release channels on the ER are located approximately 50–100 nm from TMEM16a on the PM (Pages et al., 2019). In this microdomain, confocal microscopy cannot easily distinguish the distinct localization of TMEM16a/ IP_3R , despite their localization on different membranes. However, STED super-resolution microscopy provides a much higher spatial resolution, achieving 20–80 nm to enable the differentiation of proteins within 20–80 nm of each other. Data using STED microscopy, suggest that the microdomain between apical ER IP_3R and apical PM TMEM16a is disrupted in the disease model. The severe fragmentation of ER observed in EM images from DMXAA-treated animals also is consistent with an alteration in the relationship between ER and other intracellular domains. The disruption of the relative localization of these channels could conceivably result in diminished TMEM16a activity, if activation is dependent on the local $[\text{Ca}^{2+}]$ in its vicinity. Our data showing that the slow Ca^{2+} buffer EGTA eliminates TMEM16a activation in the disease model, but that currents can still be evoked in vehicle-treated controls is consistent with the activation of TMEM16a by the local Ca^{2+} signal surrounding the channel rather than the global cytoplasmic Ca^{2+} signal (Jin et al., 2016; Shah et al., 2020; Wang et al., 2020). Thus, the disruption of this apical microdomain likely alters the local Ca^{2+} signal that TMEM16a experiences leading to reduced activation and fluid secretion.

While changes in cytosolic $[\text{Ca}^{2+}]$ are vitally important for stimulating ion flux and hence fluid secretion, Ca^{2+} is also critical for numerous other physiological processes in salivary gland acinar cells. We focused on the potential effects of the dysregulated Ca^{2+} signal on mitochondrial morphology and function. Secretion is an energy-demanding process, necessitating a constant supply of ATP for numerous functions, including vesicle transport, protein modification, membrane fusion, and maintaining ion gradients. For example, the Na^+/K^+ ATPase pump generates the Na^+ gradient, driving Cl^- transport into the cytosol of acinar cells through NKCC1, and SERCA pumps replenish ER Ca^{2+} levels. In this context, mitochondria are essential as they provide ATP, regulate Ca^{2+} homeostasis, supply metabolic intermediates, and coordinate with the ER to orchestrate cellular functions (Denton, 2009; Detmer and Chan, 2007). Notably, recent studies have highlighted that mitochondria are abundant and display varied positioning and dynamics in salivary gland cells (Porat-Shliom et al., 2019). In SS patients, there are notable alterations in mitochondrial structure, including swelling and disrupted cristae (Barrera et al., 2021; Li et al., 2022). Correspondingly, mitochondrial-related genes, particularly those involved in metabolism, dynamics, and the electron transport complex, are significantly affected (Li et al., 2022). Our data, employing fluorescent immunostaining and EM, mirrors these findings in DMXAA-treated animals. We observed that mitochondrial morphology is altered such that mitochondria are more swollen and rounded, with dispersed cristae, similar to that reported in human SS patients (Barrera et al., 2021). Since optimal mitochondrial bioenergetics are also dependent on Ca^{2+} signals, we assessed mitochondrial function by measuring the mitochondrial membrane potential ($\Delta\Psi_m$) using a membrane potential sensitive probe and the OCR using Seahorse technology. Our results show that in the SS mouse model, $\Delta\Psi_m$, which is critical for ATP synthesis, is diminished (Figure 10C). While the ATP-linked OCR remained unchanged, both the basal and maximal OCR were reduced. This suggests that mitochondrial functionality is compromised in the disease model, indicating a decreased capacity to respond to additional cellular stress. An intriguing question arises from these findings: are defects in the function of mitochondria a primary cause of fluid secretion loss in SS, or alternatively is this a consequence of disrupted $[\text{Ca}^{2+}]$ regulation? Moreover, DNA from damaged mitochondria can activate the cGAS/STING pathway, leading to inflammation (Decout et al., 2021; Gao et al., 2013). This implies that compromised mitochondria in early SS stages could trigger prolonged inflammation through the STING pathway, potentially contributing to SS progression. Understanding these mechanisms is crucial for developing effective treatments to halt or slow the progression of SS.

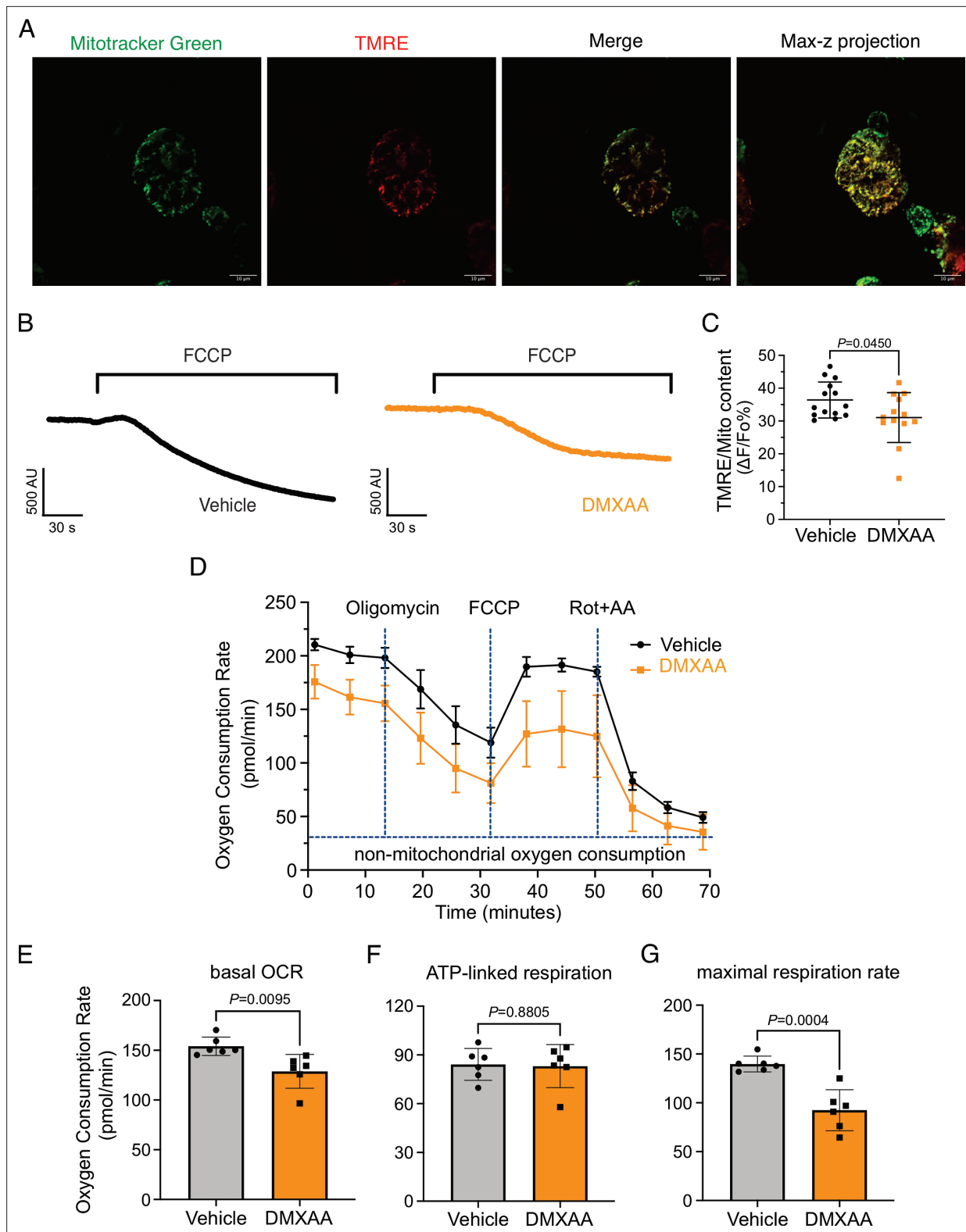


Figure 10. Mitochondrial bioenergetics are compromised in the 5,6-Dimethyl-9-oxo-9H-xanthene-4-acetic acid (DMXAA)-treated Sjögren's syndrome (SS) model. **(A)** Mitochondria in the isolated acinar cells were labeled by the MitoTracker Green and co-stained with mitochondrial membrane potential dye, TMRE (red). The merged image shows the colocalization of both dyes, with maximal z-stack projection throughout the acinar cells. **(B)** Representative changes in mitochondrial membrane potential following FCCP-induced depolarization. The vehicle is shown in black; the SS mouse model is in orange. **(C)** The quantification was achieved by the difference of Tetramethylrhodamine, ethyl ester (TMRE) normalized to MitoTracker Green.

Figure 10 continued on next page

Figure 10 continued

Each dot is the mean of 10 cells from one experiment. Vehicle: n=14 and SS mouse model: n=13 from 3 mice. **(D)** Real-time mitochondrial respiration function was assessed in isolated acinar cells from the vehicle (black) and SS mouse model (orange) using the Seahorse XFe96 extracellular flux analyzer, in response to the pharmacological mito stress (oligomycin, FCCP, rotenone, and antimycin). Vehicle: n=59 and SS mouse model: n=32 from 6 mice. **(E–G)** Mitochondrial respiration function parameters were quantified by oxygen consumption rate (OCR) subtracted the non-mitochondrial OCR for **(E)** basal respiration rate, **(F)** ATP-linked respiration rate, and **(G)** maximal respiration rate. Mean \pm SD. Unpaired two-tailed t-test. Source data is included in **Figure 10—source data 1**.

The online version of this article includes the following source data and figure supplement(s) for figure 10:

Source data 1. Raw mitochondrial bioenergetics data.

Figure supplement 1. Reduction of the basal tetramethylrhodamine, ethyl ester (TMRE) fluorescence in 5,6-Dimethyl-9-oxo-9H-xanthene-4-acetic acid (DMXAA)-treated animals.

Figure supplement 1—source data 1. Raw fluorescence data.

Materials and methods

Key resources table

Reagent type (species) or resource	Designation	Source or reference	Identifiers	Additional information
Strain, strain background (mouse)	C57BL/6 J	Jackson Laboratory	RRID:IMSR_JAX:000664	8–10 weeks-old female mice
Strain, strain background (mouse)	B6.129-Bhlha15 ^{tm3(cre)ERT2} Sicz/J	Jackson Laboratory	RRID:IMSR_JAX:029228	
Strain, strain background (mouse)	B6J.Cg-Gt(ROSA)26Sor ^{tm95.1} (CAG-GCaMP6b) ^{Hze} /MwarJ	Jackson Laboratory	RRID:IMSR_JAX:028865	
Chemical compound, drug	5,6-dimethyl-9-oxo-9H-xanthene-4-acetic acid (DMXAA)	Vadimezan	GC16280	Stock conc.: 10 mg/ml
Chemical compound, drug	Endotoxin 7.5% sodium bicarbonate solution	Sigma-Aldrich	S8761	Working conc.: 5%
Chemical compound, drug	Pilocarpine	Millipore Sigma	P6503	Stock conc.: 5.63 mg/ml Working conc.: 1:100
Antibody	Rabbit polyclonal TMEM16a antibody	Abcam	ab84115	WB: 1:1000 IHC: 1:250
Antibody	Mouse monoclonal alpha 1 Sodium Potassium ATPase antibody	Abcam	ab2872	IHC: 1:250
Antibody	Rabbit monoclonal alpha 1 Sodium Potassium ATPase antibody	Abcam	ab76020	IHC: 1:500
Antibody	Mouse monoclonal ATP5A antibody [15H4C4]	Abcam	ab14748	IHC: 1:500
Antibody	Rabbit monoclonal Aquaporin 5 antibody	Abcam	ab239904	WB: 1:1000 IHC: 1:500
Antibody	Rabbit monoclonal STING antibody (D2P2F)	Cell signaling Technology	#13647	WB: 1:1000 IHC: 1:500
Antibody	Rabbit polyclonal IP ₃ R2 antibody (D2P2F)	PMID:33093175		WB: 1:1000 IHC: 1:200
Antibody	Mouse monoclonal IP ₃ R3 antibody (D2P2F)	BD Transduction Laboratory	610313	WB: 1:1000 IHC: 1:400
Antibody	Mouse monoclonal Actin antibody	Millipore Sigma	A2228	WB: 1:10000
Antibody	Donkey anti-rabbit Alexa 488	ThermoFisher Scientific	A-21206	IHC: 1:500
Antibody	Donkey anti-mouse Alexa 594	ThermoFisher Scientific	A-21203	IHC: 1:500
Antibody	Goat anti-rabbit IgG (H&L)	Invitrogen	SA53557	WB: 1:10000
Antibody	Goat anti-mouse IgG (H&L)	Invitrogen	SA535521	WB: 1:10000
Chemical compound, drug	4',6-Diamidino-2-phenylindol (DAPI)	ThermoFisher Scientific	#62248	IHC: 1:1000
Chemical compound, drug	MitoTracker Green FM	InvitrogenTM	M7514	Working conc.: 500 nM
Chemical compound, drug	Tetramethylrhodamine, ethyl ester (TMRE)	ThermoFisher Scientific	T669	Working conc.: 20 nM
Chemical compound, drug	Oligomycin	Millipore Sigma	O4876	Working conc.: 4 µg/ml
Chemical compound, drug	Carbonyl cyanide-p-trifluoromethoxyphenylhydrazone (FCCP)	Millipore Sigma	C2920	Working conc.: 2 µM
Chemical compound, drug	Rotenone	Millipore Sigma	R8875	Working conc.: 2 µM
Chemical compound, drug	Antimycin	Millipore Sigma	A8674	Working conc.: 2 µM
Other	Collagenase Type II	Worthington Biochemical	LS004204	Working conc.: 0.2 mg/ml Reference: https://doi.org/10.1074/jbc.M406201200
Other	Tamoxifen	Sigma-Aldrich	T5648	Reference: https://doi.org/10.7554/eLife.66170v
Software, algorithm	FIJI/Image	Fiji (imagej.net)		
Software, algorithm	Prism	GraphPad		

All animal procedures were approved by the University of Rochester Committee on Animal

Resources (UCAR-2001-214E).

Animals

The murine model of Sjögren's syndrome was established through the induction of the STING pathway (*Bagavant and Deshmukh, 2020*). Briefly, 8–10 weeks old female C57BL/6 J wild-type (WT) mice (Jackson Laboratory; Jax 000664) received subcutaneous injections of DMXAA (Vadimezan; GC16280) at a concentration of 25 mg/kg of body weight on both day 0 and day 21 of the experimental timeline (see *Figure 1*). The control mouse received vehicle (5% sodium bicarbonate; Sigma-Aldrich; S8761), the DMXAA solvent at the corresponding time points. Experiments were performed on day 28 of the experimental timeline. Animals had access to water and were fed ad libitum. All animal procedures were approved by the University of Rochester Committee on Animal Resources (UCAR-2001-214E).

Evaluation of saliva production

The mice were fasted for 2 hr prior to the evaluation of saliva production. The mice were anesthetized with a solution containing Ketamine (10 mg/mL) and Xylazine (1 mg/mL) by intraperitoneal injection (IP) at a dose of 7 μ l/gm body weight over 2 min. The mouse was placed on a heating pad at 37°C during experimentation. A Salimetrics Children's swab (Salimetrics; Cat. no. 5001.05) was placed within the oral cavity of each mouse. The mice were administered the muscarinic agonist pilocarpine (0.375 mg/kg body weight; Millipore Sigma; P6503) by IP injection. Two minutes after the pilocarpine injection, saliva was collected for the following 15 min. The saliva absorbed was subsequently separated from the moist swab through centrifugation at 10,000 rpm for 1 min. The measurement of saliva weight served as a quantitative evaluation of the efficacy of whole saliva secretion. To measure neurotransmitter-stimulated saliva secretion more directly, the mouse was anesthetized as previously described (*Takano et al., 2021*) and a surgical incision was made in the skin to expose the submandibular gland (SMG). The surrounding connective tissue was excised to facilitate positioning within a custom-made 3D-printed gland holder. A pair of stimulation electrodes were attached to the duct bundle and the SMG. The pre-weighed filter paper was positioned within the oral cavity of the mouse to capture saliva secretion. Secretion was initiated by electrical stimulation sequences generated by a stimulus isolator (Iso-flex, A.M.P.I.) set at 5 mA, 200 ms, at frequencies of 1, 3, 5, 7, and 10 Hz with train frequency and duration (typically 1 min) controlled by a train generator (DG2A, Warner Instruments). The interval between each stimulus was 3 min. After stimulation, the filter paper was removed and weighed. The difference between the weight of filter paper before and after the electrode stimulation represented the saliva produced by the respective salivary gland during the given stimulation period.

In vivo Ca²⁺ imaging

To generate mice expressing a fluorescent Ca²⁺ indicator in exocrine acinar cells, homozygous mice expressing the fast genetically encoded Ca²⁺ indicator GCaMP6f (B6J.Cg-Gt(ROSA)26Sor^{tm95.1(CAG-GCaMP6f)Hze/MwarJ}) floxed by a STOP cassette, were crossed with heterozygous tamoxifen-inducible Mist1 Cre mice (B6.129-Bhlha15^{tm3(cre/ERT2)Skz/J}) A week before the DMXAA or 5% sodium bicarbonate injections, tamoxifen (Sigma-Aldrich; T5648) was given to the mice via oral gavage at a dose of 0.25 mg/g of body weight for three consecutive days to excise the loxP sites flanking the STOP codon allowing expression of the Ca²⁺ indicator within salivary glands. The mice were anesthetized and gland-exposed, as described previously (*Takano et al., 2021; Takano and Yule, 2022*). The immobilized gland was secured within the holder using a cover glass and maintained in Hank's salt solution (HBSS). Ca²⁺ imaging was conducted in vivo via two-photon microscopy using an Olympus FVMPE-RS system equipped with an Insight X3 pulsed laser (Spectra-Physics) utilizing a heated (OKOLab COL2532) 25 x water immersion lens (Olympus XLPlan N 1.05 W MP). GCaMP6f was excited at 950 nm and emission collected between 495–540 nm, with images captured at 0.5 s intervals following stimulation for 10 s with 3 min between stimulation periods. Statistical analyses were performed with two-way ANOVA with multiple comparisons using Prism (GraphPad) as indicated in the figure legends.

Immunofluorescent staining for sliced tissue

Following verification of decreased saliva secretion in mice, glands were processed for immunocytochemistry. Briefly, the isolated salivary glands were fixed in 4% paraformaldehyde at 4°C overnight. The fixed gland was processed, embedded in paraffin, and subsequently sliced into 5 μ m thick

sections. Two temperature-induced antigen retrieval protocols were used either based on HIER buffer (10 mM Tris-base, 1 mM EDTA-dehydrate, pH 9.2) or sodium citrate buffer (10 mM sodium citrate, 0.05% Tween 20, pH 6.0). Gland sections were blocked with the 10% donkey serum in 0.2% PBSA (PBS + BSA) at room temperature (RT) for 1 hr. Sections were incubated with the primary antibody at 4°C overnight (TMEM16a (Millipore Sigma; P6593; 1:250), Na⁺/K⁺ ATPase (Abcam; ab2872; 1:250), ATP5A (Abcam; ab14748; 1:500), AQP5 (Abcam; ab239904; 1:500), STING (Cell signaling Technology, Cat. 13647; 1:500)). Following washing, the sections were then incubated with the secondary antibody at RT for 1 hr (Donkey anti-rabbit Alexa 488 (Thermo Fisher Scientific; A-21206; 1:500), Donkey anti-mouse Alexa 594 (Thermo Fisher Scientific; A-21203; 1:500)). Nuclei were identified by incubation in DAPI (Thermo Fisher Scientific; Cat. 62248; 1:1000) at RT for 5 min. Tissue sections were mounted using Immu-Mount solution on a slide and then sealed under a coverslip. Images were acquired by Olympus FV1000MP confocal microscopy employing an Olympus UPlanSApo 60 x oil immersion objective. The analysis of images was performed using FIJI software. Statistical analyses were performed with a t-test using Prism (GraphPad) as indicated in the figure legends.

Patch clamp electrophysiology

Acinar cells were allowed to adhere to Cell-Tak-coated glass coverslips for 15 min before experimentation. Coverslips were transferred to a chamber containing extracellular bath solution (155 mM tetraethylammonium chloride to block K⁺ channels, 2 mM CaCl₂, 1 mM MgCl₂, 10 mM HEPES, pH 7.2). Cl⁻ currents in individual cells were measured in the whole cell patch clamp configuration using pClamp 9 and an Axopatch 200B amplifier (Molecular Devices). Recordings were sampled at 2 kHz and filtered at 1 kHz. Pipette resistances were 3–5 MΩ, and seal resistances were greater than 1 GΩ. Pipette solutions (pH 7.2) contained 60 mM tetraethylammonium chloride, 90 mM tetraethylammonium glutamate, 10 mM HEPES, 1 mM HEDTA (N-(2-hydroxyethyl) ethylenediamine-N, N', N'-triacetic acid) and 20 μM CaCl₂ were used to mimic physiological buffering and basal [Ca²⁺]_i conditions (~100 nM Ca²⁺). Free [Ca²⁺]_i was estimated using Maxchelator freeware. Agonists were directly perfused onto individual cells using a multibarrel perfusion pipette. The pipette solution for the increased basal [Ca²⁺]_i contained hEDTA and a free [Ca²⁺]_i of 500 nM, 1 mM, or 5 mM to induce calcium-activated Cl⁻ currents without the addition of any agonists. Experiments comparing EGTA, BAPTA, and HEDTA effects upon chloride currents induced by CCh stimulation contained 5 mM free concentrations of the chelator and 100 nM free [Ca²⁺]_i in the patch pipette. Chloride currents following agonist application were monitored with a single voltage step to 80 mV from a holding potential of -80 mV every second until current magnitudes reached a plateau. Current-voltage relationships were obtained by 20 mV incremental steps between -80 mV and 120 mV from a holding potential of -50 mV.

STED microscopy

3D STED microscopy was performed using an Abberior Instruments Expert Line STED microscope equipped with an Olympus UPLSAPO 100x/1.4NA oil immersion objective. Briefly, lobules <1 mm were isolated following injection of saline beneath the capsule with a 29-gauge needle. The connecting tissue was digested in 0.1 mg/ml collagenase containing image buffer at 37°C for 5 min. Then isolated lobules were fixed in 100% methanone at -20°C for 5 min, and subsequently were blocked with 10% BSA in 0.1% PBST (PBS + 0.1% Tween20) at RT for 1 hr with gentle shaking. Isolated lobules were incubated with primary antibodies overnight at 4 °C (TMEM16a (Millipore Sigma; P6593; 1:300), IP₃R3 (BD Transduction Laboratory; Cat. 610313; 1:200)). After being washed with 0.1% PBST, the membranes were incubated with secondary antibodies at RT for 1 hr (STAR RED, goat anti-rabbit IgG secondary antibody (Abberior, Cat#STRED-1001–500 UG; 1:1000), Alexa Fluor 594 anti-rabbit IgG secondary antibody (Molecular Probes Cat#A-11037; 1:1000)). The tissue was mounted on the slides with Prolong Gold antifade reagent (Invitrogen; Cat. P36930). Sequential confocal and STED images were obtained following excitation of Alexa Fluor 594 and STAR RED by 594 and 640 nm lasers, respectively. Both fluorophores were depleted in three dimensions with a 775 nm pulsed STED laser. Z-stacks were obtained by collecting images at 50 nm intervals using the 3D STED mode. Rescue STED was employed to minimize the light dosage. Blend mode depth projection images were generated and fluorophore volumes and interfaces between these volumes were analyzed using FIJI.

Seahorse XF cell mito stress assay

Isolated SMGs were finely minced and subsequently resuspended in a solution composed of 0.5% bovine serum albumin (BSA) in Hank's balanced salt solution (HBSS). To isolate acinar cells, the minced tissue was incubated in 0.5% BSA/HBSS containing 0.2 mg/ml of collagenase type II (Worthington; LS004204) for 30 min. Following this incubation, the suspension of cells was centrifuged at 500 rpm for 1 min and the cellular pellet was then resuspended in 40 µg/ml of Trypsin inhibitor (Millipore; Cat. 65035) to terminate further digestion. The function of mitochondria was assessed in isolated acinar cells by measurement of oxygen consumption rate (OCR) employing a Seahorse XF Cell Mito Stress Test system (Agilent, USA). Briefly, Equal sized SMG cell pellets were suspended in buffer and 10 µl of the acinar cell suspension was seeded into individual wells of Seahorse cell culture microplates coated with 10 µL of Cell-Tak (0.25 mg/ml) and the OCR was determined utilizing the Seahorse XFe96 extracellular flux analyzer following sequential exposure to 4 µg/ml oligomycin (Millipore Sigma; O4876), 4 µM carbonyl cyanide-4 (trifluoromethoxy)phenylhydrazone (FCCP; Millipore Sigma; C2920), and 0.5 µM rotenone/antimycin (Millipore Sigma; R8875; A8674) to measure the quantification of basal respiration, ATP-linked respiration, and maximum respiration rate, respectively. Statistical analyses were performed with a t-test using Prism (GraphPad) as indicated in the figure legends.

Measurement of mitochondrial membrane potential

Isolated SMG acinar cells were loaded with 20 nM Tetramethylrhodamine, Ethyl Ester (TMRE; ThermoFisher Scientific: T669), and 1 µM of MitoTracker Green (Invitrogen; M7514). Fluorescence of both TMRE and MitoTracker Green was captured simultaneously using an inverted epifluorescence Nikon microscope with a 40 x oil immersion objective. The TMRE fluorescence was excited at 560 nm and emitted light collected at 574 nm; MitoTracker Green was excited at 488 nm and emitted light collected at 530 nm. Images were obtained every 1 s with an exposure of 20 ms and 4 × 4 binning using a digital camera controlled by TILL Photonics, TILLvision software. The acinar cells were exposed to 4 µM FCCP for 3 mins by perfusion to rapidly dissipate the membrane potential. Mitochondrial membrane potential was quantified as the change in the ratio of TMRE/MitoTracker Green fluorescence before and after the administration of FCCP. Statistical analyses were performed with a t-test using Prism (GraphPad) as indicated in the figure legends.

Western blotting

Finely minced salivary glands were homogenized in a lysis buffer supplemented with protease inhibitor cocktail (Complete mini; Roche Diagnostics) for 16–20 strokes. After incubating on ice for 30 min, solubilized proteins were separated by centrifugation at 13,000 rpm at 4°C for 30 min. 10 µg of protein lysate was loaded on 7.5–12% SDS- polyacrylamide gels. Subsequently, the proteins were transferred to PVDF membranes at a voltage of 35 V at 4 °C overnight. The membrane was blocked with 5% non-fat skimmed milk in TBST (50 mM Tris-HCl, pH 7.5 with 0.1% Tween20) at RT for 1 hr and subsequently incubated with primary antibodies overnight at 4 °C (Actin (Millipore Sigma; A2228; 1:10000), IP₃R2 (Antibody Research Corporation; 1:1000), IP₃R3 (BD Transduction Laboratory; Cat. 610313; 1:1000), TMEM16a (Abcam; ab84115; 1:1000)). After being washed with 0.1% TBST, the membranes were incubated with secondary antibodies at RT for 1 hr (Goat anti-rabbit IgG (H&L) (Invitrogen; SA535571; 1:10000), Goat anti-mouse IgG (H&L) (Invitrogen; SA535521; 1:10000)). Protein band intensity from western blotting was quantified by FIJI. The relative ratio of DMXAA-treated/vehicle control was calculated in Excel. Lastly, graphical generation and statistics were performed with a t-test using Prism (GraphPad) as indicated in the figure legends.

Acknowledgements

The authors gratefully acknowledge the University of Rochester's Center for Advanced Microscopy and Nanoscopy (CALMN) for providing access to Multiphoton microscopy for in vivo live imaging and STED super-resolution microscopy, and for Center for Advanced Research Technologies (CART) for the Electron & cryo Microscopy Resource. We also thank the Flow Cytometry Resource (FCR) for its support with the mitochondrial stress assay. Special thanks to Dr. Paul Brooks for sharing Seahorse Technology XF analyzers and for engaging in discussions for optimization of experiments. Thanks to Dr. Catherine Ovitt for her instruction on tissue staining techniques. Additionally, we wish to express

our appreciation to all members of the Yule laboratory for their invaluable feedback, discussions, and assistance, which have been essential in advancing this study. The work was supported by a grant from NIH (NIDCR) DE014756 (to DIY).

Additional information

Funding

Funder	Grant reference number	Author
National Institute of Dental and Craniofacial Research	DE014756	Takahiro Takano

The funders had no role in study design, data collection and interpretation, or the decision to submit the work for publication.

Author contributions

Kai-Ting Huang, Investigation, Writing - original draft; Larry E Wagner, Data curation, Investigation; Takahiro Takano, Xiao-Xuan Lin, Harini Bagavant, Investigation; Umesh Deshmukh, Investigation, Methodology; David I Yule, Conceptualization, Formal analysis, Supervision, Funding acquisition, Project administration

Author ORCIDs

Kai-Ting Huang  <https://orcid.org/0000-0003-3138-3406>

Larry E Wagner  <https://orcid.org/0000-0002-5631-8697>

David I Yule  <https://orcid.org/0000-0002-6743-0668>

Ethics

All animal procedures were approved by the University of Rochester Committee on Animal Resources (UCAR-2001-214E).

Peer review material

Reviewer #1 (Public review): <https://doi.org/10.7554/eLife.97069.3.sa1>

Reviewer #2 (Public review): <https://doi.org/10.7554/eLife.97069.3.sa2>

Reviewer #3 (Public review): <https://doi.org/10.7554/eLife.97069.3.sa3>

Author response <https://doi.org/10.7554/eLife.97069.3.sa4>

Additional files

Supplementary files

- MDAR checklist

Data availability

All data generated and analyzed in this study are included in the manuscript and supporting files.

References

- Bagavant H**, Deshmukh US. 2020. Protocols for experimental sjögren's syndrome. *Current Protocols in Immunology* **131**:e114. DOI: <https://doi.org/10.1002/cpim.114>, PMID: 33252847
- Barrera MJ**, Aguilera S, Castro I, Carvajal P, Jara D, Molina C, González S, González MJ. 2021. Dysfunctional mitochondria as critical players in the inflammation of autoimmune diseases: Potential role in Sjögren's syndrome. *Autoimmunity Reviews* **20**:102867. DOI: <https://doi.org/10.1016/j.autrev.2021.102867>, PMID: 34118452
- Brito-Zerón P**, Baldini C, Bootsma H, Bowman SJ, Jonsson R, Mariette X, Sivils K, Theander E, Tzioufas A, Ramos-Casals M. 2016. Sjögren syndrome. *Nature Reviews. Disease Primers* **2**:16047. DOI: <https://doi.org/10.1038/nrdp.2016.47>, PMID: 27383445
- Carpenter GH**. 2013. The secretion, components, and properties of saliva. *Annual Review of Food Science and Technology* **4**:267–276. DOI: <https://doi.org/10.1146/annurev-food-030212-182700>, PMID: 23464573
- Catalán MA**, Kondo Y, Peña-Munzenmayer G, Jaramillo Y, Liu F, Choi S, Crandall E, Borok Z, Flodby P, Shull GE, Melvin JE. 2015. A fluid secretion pathway unmasked by acinar-specific Tmem16A gene ablation in the adult mouse salivary gland. *PNAS* **112**:2263–2268. DOI: <https://doi.org/10.1073/pnas.1415739112>, PMID: 25646474

- Cerón S**, North BJ, Taylor SA, Leib DA. 2019. The STING agonist 5,6-dimethylxanthenone-4-acetic acid (DMXAA) stimulates an antiviral state and protects mice against herpes simplex virus-induced neurological disease. *Virology* **529**:23–28. DOI: <https://doi.org/10.1016/j.virol.2019.01.006>, PMID: 30648635
- Csordás G**, Renken C, Várnai P, Walter L, Weaver D, Buttler KF, Balla T, Mannella CA, Hajnóczky G. 2006. Structural and functional features and significance of the physical linkage between ER and mitochondria. *The Journal of Cell Biology* **174**:915–921. DOI: <https://doi.org/10.1083/jcb.200604016>, PMID: 16982799
- Decout A**, Katz JD, Venkatraman S, Ablasser A. 2021. The cGAS-STING pathway as a therapeutic target in inflammatory diseases. *Nature Reviews. Immunology* **21**:548–569. DOI: <https://doi.org/10.1038/s41577-021-00524-z>, PMID: 33833439
- Denton RM**. 2009. Regulation of mitochondrial dehydrogenases by calcium ions. *Biochimica et Biophysica Acta* **1787**:1309–1316. DOI: <https://doi.org/10.1016/j.bbabi.2009.01.005>, PMID: 19413950
- de Paula F**, Teshima THN, Hsieh R, Souza MM, Nico MMS, Lourenco SV. 2017. Overview of human salivary glands: Highlights of morphology and developing processes. *Anatomical Record* **300**:1180–1188. DOI: <https://doi.org/10.1002/ar.23569>, PMID: 28192873
- Detmer SA**, Chan DC. 2007. Functions and dysfunctions of mitochondrial dynamics. *Nature Reviews. Molecular Cell Biology* **8**:870–879. DOI: <https://doi.org/10.1038/nrm2275>, PMID: 17928812
- Duchen MR**. 2000. Mitochondria and calcium: from cell signalling to cell death. *The Journal of Physiology* **529 Pt 1**:57–68. DOI: <https://doi.org/10.1111/j.1469-7793.2000.00057.x>, PMID: 11080251
- Eisner D**, Neher E, Taschenberger H, Smith G. 2023. Physiology of intracellular calcium buffering. *Physiological Reviews* **103**:2767–2845. DOI: <https://doi.org/10.1152/physrev.00042.2022>, PMID: 37326298
- Futatsugi A**, Nakamura T, Yamada MK, Ebisui E, Nakamura K, Uchida K, Kitaguchi T, Takahashi-Iwanaga H, Noda T, Aruga J, Mikoshiba K. 2005. IP3 receptor types 2 and 3 mediate exocrine secretion underlying energy metabolism. *Science* **309**:2232–2234. DOI: <https://doi.org/10.1126/science.1114110>, PMID: 16195467
- Gao P**, Ascano M, Zillinger T, Wang W, Dai P, Serganov AA, Gaffney BL, Shuman S, Jones RA, Deng L, Hartmann G, Barchet W, Tuschl T, Patel DJ. 2013. Structure-function analysis of STING activation by c[G(2',5')pA(3',5')p] and targeting by antiviral DMXAA. *Cell* **154**:748–762. DOI: <https://doi.org/10.1016/j.cell.2013.07.023>, PMID: 23910378
- Gao Y**, Chen Y, Zhang Z, Yu X, Zheng J. 2020. Recent advances in mouse models of sjögren's syndrome. *Frontiers in Immunology* **11**:1158. DOI: <https://doi.org/10.3389/fimmu.2020.01158>, PMID: 32695097
- Gresz V**, Horvath A, Gera I, Nielsen S, Zelles T. 2015. Immunolocalization of AQP5 in resting and stimulated normal labial glands and in Sjögren's syndrome. *Oral Diseases* **21**:e114–e120. DOI: <https://doi.org/10.1111/odi.12239>, PMID: 24661359
- Harwig MC**, Viana MP, Egnér JM, Harwig JJ, Widlansky ME, Rafelski SM, Hill RB. 2018. Methods for imaging mammalian mitochondrial morphology: A prospective on MitoGraph. *Analytical Biochemistry* **552**:81–99. DOI: <https://doi.org/10.1016/j.ab.2018.02.022>, PMID: 29505779
- Hogan MC**, Stary CM, Balaban RS, Combs CA. 2005. NAD(P)H fluorescence imaging of mitochondrial metabolism in contracting *Xenopus* skeletal muscle fibers: effect of oxygen availability. *Journal of Applied Physiology* **98**:1420–1426. DOI: <https://doi.org/10.1152/jappphysiol.00849.2004>, PMID: 15591295
- Huijser E**, Bodewes ILA, Lourens MS, van Helden-Meeuwse CG, van den Bosch TPP, Grashof DGB, van de Werken HJG, Lopes AP, van Roon JAG, van Daele PLA, Brkic Z, Dik WA, Versnel MA. 2022. Hyperresponsive cytosolic DNA-sensing pathway in monocytes from primary Sjögren's syndrome. *Rheumatology* **61**:3491–3496. DOI: <https://doi.org/10.1093/rheumatology/keac016>, PMID: 35022662
- Humphrey SP**, Williamson RT. 2001. A review of saliva: Normal composition, flow, and function. *The Journal of Prosthetic Dentistry* **85**:162–169. DOI: <https://doi.org/10.1067/mpr.2001.113778>
- Jin X**, Shah S, Du X, Zhang H, Gamper N. 2016. Activation of Ca(2+)-activated Cl(-) channel ANO1 by localized Ca(2+) signals. *The Journal of Physiology* **594**:19–30. DOI: <https://doi.org/10.1113/jphysiol.2014.275107>, PMID: 25398532
- Jonsson R**, Brokstad KA, Jonsson MV, Delaleu N, Skarstein K. 2018. Current concepts on Sjögren's syndrome - classification criteria and biomarkers. *European Journal of Oral Sciences* **126 Suppl 1**:37–48. DOI: <https://doi.org/10.1111/eos.12536>, PMID: 30178554
- Katona M**, Bartók Á, Nichtova Z, Csordás G, Berezhnaya E, Weaver D, Ghosh A, Várnai P, Yule DI, Hajnóczky G. 2022. Capture at the ER-mitochondrial contacts licenses IP3 receptors to stimulate local Ca2+ transfer and oxidative metabolism. *Nature Communications* **13**:6779. DOI: <https://doi.org/10.1038/s41467-022-34365-8>
- Kiripolsky J**, Shen L, Liang Y, Li A, Suresh L, Lian Y, Li QZ, Gaile DP, Kramer JM. 2017. Systemic manifestations of primary Sjögren's syndrome in the NOD.B10Sn-H2/J mouse model. *Clinical Immunology* **183**:225–232. DOI: <https://doi.org/10.1016/j.clim.2017.04.009>
- Lee MG**, Xu X, Zeng W, Diaz J, Wojcikiewicz RJH, Kuo TH, Wuytack F, Racymaekers L, Muallem S. 1997. Polarized expression of Ca2+ channels in pancreatic and salivary gland cells. *Journal of Biological Chemistry* **272**:15765–15770. DOI: <https://doi.org/10.1074/jbc.272.25.15765>
- Lee BH**, Gauna AE, Pauley KM, Park YJ, Cha S. 2012. Animal models in autoimmune diseases: lessons learned from mouse models for Sjögren's syndrome. *Clinical Reviews in Allergy & Immunology* **42**:35–44. DOI: <https://doi.org/10.1007/s12016-011-8288-5>, PMID: 22105703
- Li N**, Li Y, Hu J, Wu Y, Yang J, Fan H, Li L, Luo D, Ye Y, Gao Y, Xu H, Hai W, Jiang L. 2022. A link between mitochondrial dysfunction and the immune microenvironment of salivary glands in primary sjogren's syndrome. *Frontiers in Immunology* **13**:845209. DOI: <https://doi.org/10.3389/fimmu.2022.845209>, PMID: 35359935

- Martínez J**, Marmisolle I, Tarallo D, Quijano C. 2020. Mitochondrial bioenergetics and dynamics in secretion processes. *Frontiers in Endocrinology* **11**:319. DOI: <https://doi.org/10.3389/fendo.2020.00319>, PMID: 32528413
- Mavragani CP**, Basiaga ML. 2014. Sjögren Syndrome. Canadian Medical Association. DOI: <https://doi.org/10.1503/cmaj.122037>
- Melvin JE**, Yule D, Shuttleworth T, Begenisich T. 2005. Regulation of fluid and electrolyte secretion in salivary gland acinar cells. *Annual Review of Physiology* **67**:445–469. DOI: <https://doi.org/10.1146/annurev.physiol.67.041703.084745>, PMID: 15709965
- Navaratnarajah T**, Anand R, Reichert AS, Distelmaier F. 2021. The relevance of mitochondrial morphology for human disease. *The International Journal of Biochemistry & Cell Biology* **134**:105951. DOI: <https://doi.org/10.1016/j.biocel.2021.105951>, PMID: 33610749
- Pages N**, Vera-Sigüenza E, Rugis J, Kirk V, Yule DI, Sneyd J. 2019. A model of [formula: see text] dynamics in an accurate reconstruction of parotid acinar cells. *Bulletin of Mathematical Biology* **81**:1394–1426. DOI: <https://doi.org/10.1007/s11538-018-00563-z>, PMID: 30644065
- Papinska J**, Bagavant H, Gmyrek GB, Sroka M, Tummala S, Fitzgerald KA, Deshmukh US. 2018. Activation of stimulator of interferon genes (STING) and sjögren syndrome. *Journal of Dental Research* **97**:893–900. DOI: <https://doi.org/10.1177/0022034518760855>, PMID: 29505322
- Papinska J**, Bagavant H, Gmyrek GB, Deshmukh US. 2020. Pulmonary involvement in a mouse model of sjögren's syndrome induced by STING activation. *International Journal of Molecular Sciences* **21**:4512. DOI: <https://doi.org/10.3390/ijms21124512>, PMID: 32630417
- Pedersen AML**, Sørensen CE, Proctor GB, Carpenter GH, Ekström J. 2018. Salivary secretion in health and disease. *Journal of Oral Rehabilitation* **45**:730–746. DOI: <https://doi.org/10.1111/joor.12664>, PMID: 29878444
- Phillips RM**. 1999. Inhibition of DT-diaphorase (NAD(P)H:quinone oxidoreductase, EC 1.6.99.2) by 5,6-dimethylxanthenone-4-acetic acid (DMXAA) and flavone-8-acetic acid (FAA): implications for bioreductive drug development. *Biochemical Pharmacology* **58**:303–310. DOI: [https://doi.org/10.1016/s0006-2952\(99\)00092-1](https://doi.org/10.1016/s0006-2952(99)00092-1), PMID: 10423172
- Porat-Shliom N**, Harding OJ, Malec L, Narayan K, Weigert R. 2019. Mitochondrial populations exhibit differential dynamic responses to increased energy demand during exocytosis in vivo. *iScience* **11**:440–449. DOI: <https://doi.org/10.1016/j.isci.2018.12.036>, PMID: 30661001
- Ramos-Casals M**, Brito-Zerón P, Sisó-Almirall A, Bosch X. 2012. Primary Sjogren syndrome. *BMJ* **344**:e3821. DOI: <https://doi.org/10.1136/bmj.e3821>, PMID: 22700787
- Romanenko VG**, Catalán MA, Brown DA, Putzier I, Hartzell HC, Marmorstein AD, Gonzalez-Begne M, Rock JR, Harfe BD, Melvin JE. 2010. Tmem16A encodes the Ca²⁺-activated Cl⁻ channel in mouse submandibular salivary gland acinar cells. *The Journal of Biological Chemistry* **285**:12990–13001. DOI: <https://doi.org/10.1074/jbc.M109.068544>, PMID: 20177062
- Saleh J**, Figueiredo MAZ, Cherubini K, Salum FG. 2015. Salivary hypofunction: an update on aetiology, diagnosis and therapeutics. *Archives of Oral Biology* **60**:242–255. DOI: <https://doi.org/10.1016/j.archoralbio.2014.10.004>, PMID: 25463902
- Schaefer PM**, Kalinina S, Rueck A, von Arnim CAF, von Einem B. 2019. NADH autofluorescence—a marker on its way to boost bioenergetic research. *Cytometry. Part A* **95**:34–46. DOI: <https://doi.org/10.1002/cyto.a.23597>, PMID: 30211978
- Shah S**, Carver CM, Mullen P, Milne S, Lukacs V, Shapiro MS, Gamper N. 2020. Local Ca²⁺ signals couple activation of TRPV1 and ANO1 sensory ion channels. *Science Signaling* **13**:eaaw7963. DOI: <https://doi.org/10.1126/scisignal.aaw7963>, PMID: 32345727
- Shen L**, Zhang C, Wang T, Brooks S, Ford RJ, Lin-Lee YC, Kasianowicz A, Kumar V, Martin L, Liang P, Cowell J, Ambrus JL. 2006. Development of autoimmunity in IL-14 α -transgenic mice. *Journal of Immunology* **177**:5676–5686. DOI: <https://doi.org/10.4049/jimmunol.177.8.5676>, PMID: 17015757
- Shen L**, Suresh L, Li H, Zhang C, Kumar V, Pankewycz O, Ambrus JL. 2009. IL-14 α , the nexus for primary Sjögren's disease in mice and humans. *Clinical Immunology* **130**:304–312. DOI: <https://doi.org/10.1016/j.clim.2008.10.006>, PMID: 19038581
- Tabbara KF**, Vera-Cristo CL. 2000. Sjögren syndrome. *Current Opinion in Ophthalmology* **11**:449–454. DOI: <https://doi.org/10.1097/00055735-200012000-00011>, PMID: 11141640
- Takano T**, Wahl AM, Huang KT, Narita T, Rugis J, Sneyd J, Yule DI. 2021. Highly localized intracellular Ca²⁺ signals promote optimal salivary gland fluid secretion. *eLife* **10**:e66170. DOI: <https://doi.org/10.7554/eLife.66170>, PMID: 34240705
- Takano T**, Yule DI. 2022. In vivo Ca²⁺ imaging in mouse salivary glands. *BIO-PROTOCOL* **12**:e4380. DOI: <https://doi.org/10.21769/BioProtoc.4380>
- Teos LY**, Zhang Y, Cotrim AP, Swaim W, Won JH, Ambrus J, Shen L, Bebris L, Grisius M, Jang SI, Yule DI, Ambudkar IS, Alevizos I. 2015. IP3R deficit underlies loss of salivary fluid secretion in Sjögren's Syndrome. *Scientific Reports* **5**:13953. DOI: <https://doi.org/10.1038/srep13953>, PMID: 26365984
- Tsubota K**, Hirai S, King LS, Agre P, Ishida N. 2001. Defective cellular trafficking of lacrimal gland aquaporin-5 in Sjögren's syndrome. *Lancet* **357**:688–689. DOI: [https://doi.org/10.1016/S0140-6736\(00\)04140-4](https://doi.org/10.1016/S0140-6736(00)04140-4), PMID: 11247557
- Valente AJ**, Maddalena LA, Robb EL, Moradi F, Stuart JA. 2017. A simple ImageJ macro tool for analyzing mitochondrial network morphology in mammalian cell culture. *Acta Histochemica* **119**:315–326. DOI: <https://doi.org/10.1016/j.acthis.2017.03.001>, PMID: 28314612

- Wang Q**, Bai L, Luo S, Wang T, Yang F, Xia J, Wang H, Ma K, Liu M, Wu S, Wang H, Guo S, Sun X, Xiao Q. 2020. TMEM16A Ca²⁺-activated Cl⁻ channel inhibition ameliorates acute pancreatitis via the IP3R/Ca²⁺/NFκB/IL-6 signaling pathway. *Journal of Advanced Research* **23**:25–35. DOI: <https://doi.org/10.1016/j.jare.2020.01.006>
- Weiss JM**, Guérin MV, Regnier F, Renault G, Galy-Fauroux I, Vimeux L, Feuillet V, Peranzoni E, Thoreau M, Trautmann A, Bercovici N. 2017. The STING agonist DMXAA triggers a cooperation between T lymphocytes and myeloid cells that leads to tumor regression. *Oncoimmunology* **6**:e1346765. DOI: <https://doi.org/10.1080/2162402X.2017.1346765>, PMID: 29123960
- Yanfei Hu YN**, Purushotham KR, Humphreys-Beher MG. 1992. Functional changes in salivary glands of autoimmune disease-prone NOD mice. *Journal of Physiology* **263**:E607–E614. DOI: <https://doi.org/10.1152/ajpendo.1992.263.4.E607>
- Ye L**, Zeng Q, Ling M, Ma R, Chen H, Lin F, Li Z, Pan L. 2021. Inhibition of IP3R/Ca²⁺ dysregulation protects mice from ventilator-induced lung injury via endoplasmic reticulum and mitochondrial pathways. *Frontiers in Immunology* **12**:729094. DOI: <https://doi.org/10.3389/fimmu.2021.729094>, PMID: 34603302
- Zeng M**, Szymczak M, Ahuja M, Zheng C, Yin H, Swaim W, Chiorini JA, Bridges RJ, Muallem S. 2017. Restoration of CFTR activity in ducts rescues acinar cell function and reduces inflammation in pancreatic and salivary glands of mice. *Gastroenterology* **153**:1148–1159. DOI: <https://doi.org/10.1053/j.gastro.2017.06.011>, PMID: 28634110
- Zorova LD**, Popkov VA, Plotnikov EY, Silachev DN, Pevzner IB, Jankauskas SS, Babenko VA, Zorov SD, Balakireva AV, Juhaszova M, Sollott SJ, Zorov DB. 2018. Mitochondrial membrane potential. *Analytical Biochemistry* **552**:50–59. DOI: <https://doi.org/10.1016/j.ab.2017.07.009>, PMID: 28711444